Sulphide Petrology and Contribution of Subducted Sulphur in Diamondiferous Garnet-Bearing Pyroxenites from Beni Bousera (Northern Morocco)

Jean-Pierre Lorand, Sylvain Pont, Jabrane Labidi, Pierre Cartigny, Fatima El Atrassi

SULPHIDE PETROLOGY AND CONTRIBUTION OF SUBDUCTED SULPHUR IN DIAMONDIFEROUS GARNET-BEARING PYROXENITES FROM BENI BOUSERA (NORTHERN MOROCCO)

Jean-Pierre Lorand[1], Sylvain Pont[2], Jabrane Labidi[3], Pierre Cartigny[3], and Fatima El Atrassi[4]

[1]Laboratoire de Planétologie et Géodynamique à Nantes (LPG) CNRS UMR6112, Université de Nantes, Faculté des Sciences et Techniques 2 Rue de la Houssinière - BP 92208 44322 NANTES CEDEX 3 – France

[2]Institut de Minéralogie, de Physique des Matériaux, et de Cosmochimie (IMPMC) - Sorbonne Université- Muséum National d'Histoire Naturelle, UPMC Université Paris 06, CNRS UMR CNRS 7590, 61 rue Buffon, 75005 Paris, France

[3]Institut de Physique du Globe de Paris, Université Sorbonne Paris Cité, Université Paris Diderot, 1 Rue Jussieu, 75328 Paris Cedex 05, France

[4]Laboratoire G-Time, Université Libre de Bruxelles, CP 160/02, 50 Avenue F.D. Roosevelt, 1050 Brussels, Belgium

*Corresponding author : jean-pierre.lorand@univ-nantes.fr

ABSTRACT

This paper explores the unusual sulphide-graphite association of a selection of Beni Bousera garnet clinopyroxenites that initially equilibrated within the diamond stability field. Compared to common graphite-free garnet pyroxenites analysed so far, these rocks display tenfold S enrichment with concentrations up to 5550 μg/g. Fe-Ni-Cu sulphides (up to 1.5 wt.%) consist of large (up to 3 mm across), low-Ni pyrrrhotite (<0.1 wt.% Ni) of troilite composition, along with volumetrically minor chalcopyrite and pentlandite. Such assemblages are interpreted as low-temperature (<100°C) subsolidus exsolution products from homogeneous monosulphide solid solution. Troilite compositions of the pyrrhotite indicate strongly reducing conditions that are estimated to be slightly above the iron-wüstite (IW) buffer. Bulk-sulphide compositions are closer to the FeS end-member (i.e., Cu- and Ni-depleted) than other sulphide occurrences in mantle-derived pyroxenites described so far. Moreover, troilite contains trace metal microphases (Pb and Ag tellurides, molybdenite) that has never been reported before from mantle-derived garnet pyroxenites but in diamond-hosted eclogitic sulphide inclusions. Beni Bousera sulphides also show strong similarities with diamond-hosted sulphide inclusions of eclogitic affinity for a wide range of chalcophile-siderophile trace element contents. In view of the widespread molybdenite exsolution, coupled with Mo and S/Se/Te systematics of sulphide compositions (7,872<S/Se<19,776 ; 15<Se/Te<31), black-shale pyrite is a potential sedimentary component to contribute to the petrogenesis of Beni Bousera garnet clinopyroxenites. Black shales would have recycled along with cumulates from the oceanic crust in the mantle source of Beni Bousera pyroxenites. Pyrite underwent desulfidation and replacement by troïlite during subduction and prograde metamorphism, releasing its fluid mobile elements (As, Sb, Pb) while suffering minimum S loss because of the strongly reduced conditions. Taken as a whole, our body of data supports a common origin for carbon (-27‰<δ^{13}C<-17‰) and sulphur and concomitant formation of diamond and sulphides. Both elements were delivered by an extraneous sedimentary component mixed with the altered oceanic crust rocks that was involved in the genesis of Beni Bousera garnet pyroxenites, prior to a Proterozoic partial melting event.

KEYWORDS : upper mantle, garnet pyroxenites, graphite, troilite, black shales.

INTRODUCTION

Copper-nickel-iron sulphides, known as base metal sulfides (BMS) are common accessory phases in mantle-derived pyroxenites (Lorand, 1989 a,b; Sen et al., 2010; Montanini et al., 2010) and eclogites (Aulbach et al., 2009; Gréau et al., 2013). BMS are commonly included in eclogitic-type diamonds (E-type (e.g. Yefimova et al., 1983 ; Meyer, 1987; Harris, 1992; Deines & Harris, 1995; Chaussidon et al., 1987; Stachel & Harris, 2008; Thomassot et al., 2009; Aulbach et al., 2012; McDonald et al., 2017; Kempinnen et al., 2018). This association has received highly controversial explanation. Diamond formation in eclogitic substrates has been linked to copious amounts of C-bearing fluid liberated from subducted serpentinites (Aulbach et al., 2009). Although eclogitic sulphides show S isotopic compositions supporting a major contribution of recycled surface sulfur, their host diamonds display variable C and N isotopic compositions indicating different provenances for C (e.g. Deines & Harris, 1995; Thomassot et al., 2009 ; Cartigny, 2005 ; Shirey et al., 2013; Holwell et al., 2020). Interactions between reduced metal-saturated mantle rocks and oxidized carbonate-bearing subducted slab are often invoked for diamond crystallization although reduced fluids are increasingly recognized (see reviews by Cartigny, 2005 ; Stachel & Harris, 2008; Shirey et al., 2013; Holwell et al., 2020). Aulbach et al. (2019) suggested that oxidized carbon-bearing fluids can be liberated due to interaction with reduced oceanic crust. Also, BMS inclusions are so common in eclogitic diamonds that they are considered to be involved in diamond genesis, acting either as reducing agents enhancing precipitation of diamonds from oxidized carbon-bearing fluids, as nucleii for diamond crystals, or as “catalysts” enhancing carbon dissolution and precipitation from sulphide melts (e.g. Luque et al., 1998; Stachel & Harris, 2008; Shirey et al., 2013; Palyanov et al., 2007; Bataleva et al., 2019; Zdrokov et al., 2019).

Association of BMS with carbon phases remains uncommon in high-temperature, high-

pressure pyroxenite samples from the post-cratonic mantle. Montanini et al. (2010) described an occurrence of graphite associated with sulphides within garnet clinopyroxenite layers from the External Liguride ophiolite (Italy). Graphite shows typical mantle $\delta^{13}C$ values (-4.3±0.2‰ to -4.5±0.2‰; Montanini et al (2010). However, there is no evidence for a diamond precursor in these rocks which equilibrated at approximately 2.8 GPa and 1100 °C, too low in pressure for diamond formation. Here we document a new occrrence of BMS-graphite association in some garnet pyroxenites from the Beni Bousera peridotite massif (northern Morocco). Graphite was extensively studied by Slodkevitch (1980), Pearson et al., (1989, 1991) and El Atrassi et al. (2011) who provided strong evidence for precursor diamonds. Pearson et al., (1991) identified a light C-enriched isotopic signature typical of organics-rich reduced sediments (-27‰<$\delta^{13}C$<-17‰). El Atrassi et al. (2011) identified diamond microinclusions inside graphite pseudomorphs and concluded that diamond belongs to the primary paragenesis of garnet clinopyroxenites (and are not xenocrystals as suggested by Gysi et al., 2011). Hence, the Beni Bousera graphite-garnet pyroxenites may shed new light on materials that could explain the carbon-sulfur association sampled by diamonds.

This paper focuses on the petrogenesis of the BMS phases which have not yet been documented. The mineralogy of BMS allows us to constrain redox conditions while trace element geochemistry of BMS provide clues to understand the origin of sulfur. Moreover, we report an assemblage of metallic trace phases as yet unknow in mantle-derived garnet pyroxenites and eclogites, except in sulphide inclusions in diamonds. Unlike diamond-hosted sulphide inclusions, however, Beni Bousera garnet pyroxenites show large, mm-sized BMS grains that can be easily analyzed directly on polished thin sections with in-situ-techniques, without extraction and preparation mounting in polished mounts. Our sampling was extended to graphite-poor to graphite-free garnet pyroxenite samples for comparison because detailed studies of BMS on mantle-derived high-T, high-P garnet pyroxenites from orogenic peridotite massifs are still scarce.

GEOLOGICAL SETTING

The Beni Bousera orogenic lherzolite massif crops out over 75 km^2 in the Rifean cordillera (northern Morocco), at the bottom of the Sebtides unit—the lowermost crustal unit exposed of the Rif internal zones (Chalouan et al., 2008 and reference therein) (Fig. 1). There, it occurs within a southeastern-plunging antiform overlained by high-pressure, high-temperature lower-crustal units (kinzigites, HP granulites). This portion of the subcontinental lithospheric mantle (like its counterpart the Ronda massif, southern Spain) belongs to an allochthonous lithospheric domain (the Alboran domain) accreted into the internal crustal units during Alpine orogeny ; during collision, it overthrusted Mesozoic and Tertiary sedimentary rocks of the Maghrebian (Rif and Tell) continental paleomargins (Mauffret et al., 2007 ; Chalouan et al., 2008 ; Frets et al., 2014 and reference therein). According to geochronological studies of peridotites and pyroxenites, as well as their metamorphic country rocks, the Beni Bousera peridotite massif was exhumed and emplaced into the continental crust formations between 19 and 23 Ma owing to rapid extension that produced an extremely attenuated continental lithosphere in the westernmost Mediterranee (e.g., Afiri et al., 2011 ; Van Hinsberger et al., 2014 ; Frets et al., 2014).

Lherzolites (spinel and minor garnet-bearing) contain minor harzburgites and dunites as well as pyroxenites (<10% by volume) forming parallel to subparallel layers to the foliation plane of host peridotites (Kornprobst, 1969; Pearson et al., 1989, 1991; El Atrassi et al., 2011; Gysi et al., 2011; Frets et al., 2014). It is now well accepted that these massifs show a polybaric and polythermal extended petrological record from a thick basal portion of the continental lithosphere which was exhumed from 90 to to 60 km depth by a low-angle transtensional shear zone (Afiri et al., 2011 ; Frets et al., 2014 and references therein). Hence, the massif shows a strong petro-structural zoning : from SW to NE and from top to bottom these domains are (1) the Garnet and Spinel mylonite domain (2) the Ariegite subfacies domain, (3) the Ariegite to Seiland transitional domain, and (4) the Seiland subfacies domain. Pyroxenite modal compositions vary from spinel websterites in the Seiland subfacies to garnet pyroxenites (garnet clinopyroxenites and garnet websterites) forming isoclinally folded or concordant layers with sharp contacts with the peridotites in the Ariegite subfacies

(Kornprobst, 1969; Kornprobst et al., 1990; Gysi et al., 2011; El Atrassi et al., 2011; Varas-Reus et al., 2018 and references therein). Garnet–spinel mylonites (100–200 m thick) that crop out below the overlying crustal kinzigites enclose stretched and boudinaged corundum-bearing garnet pyroxenite layers (1–10cm thick) (Kornprobst et al., 1990). Garnet pyroxenites at the transition between the Garnet–Spinel mylonites and Ariegite domains include graphite garnet clinopyroxenites characterized by octahedral graphite aggregates (2 to 5 mm) interpreted as pseudomorphosed diamond (Slodkevich, 1980, Pearson et al., 1989, 1991; 1993; 1995). This interpretation was supported by the discovery of microdiamond inclusions inside graphite (El Atrassi et al., 2011). This occurrence of ultra high-pressure garnet pyroxenites provides evidence that the continental lithosphere sampled by the Beni Bousera massif was once rooted within the diamond stability facies (>4.5 GPa)(Pearson et al., 1993; El Atrassi et al., 2011, 2013).

Garnet pyroxenites share a primary mineral assemblage dominated by garnet and aluminous pyroxenes, clino- and orthopyroxene (Kornprobst, 1969 ; Kornprobst et al., 1990 ; Gysi et al., 2011 ; El Atrassi et al., 2011, 2013). Primary clinopyroxene, Cpx(I), is characterized by a ratio between jadeite and tschermak components close to or below unity, which marks these rocks as HT-HP orogenic pyroxenites rather than eclogites (Gysi et al (2011 ; El Atrassi et al., 2011, 2013). The petrogenesis of garnet pyroxenites as a whole has received considerable attention. Varas Reus et al. (2018) subdivided these rocks into three groups from their bulk-rock compositions: Groups A encompasses corundum-bearing garnet clinopyroxenites (66.1< Mg# <81.4 ; Mg# = 100 x Mg/Mg+Fe^{2+}) with elevated Al_2O_3 contents (15-17.5 wt.%); Group-B are garnet pyroxenite samples with graphite-pseudomorphs after diamond showing Al_2O_3<14 wt.% and lower Mg# (65.1–77.8). Group C are common garnet pyroxenites showing Al_2O_3 around 15 wt.% and intermediate Mg# (73.8–83.2). Because of their large range of oxygen isotope compositions (5 <$\delta^{18}O$ <9 ‰) compared to the mantle values, garnet pyroxenites were interpreted as cumulates from melting of subducted oceanic crust that was exposed to low-temperature interaction with seawater or hydrothermal fluids (Pearson et al., 1991; 1993; Kumar et al., 1996; Pearson & Nowell, 2004). Likewise, graphitized

diamond pseudomorphs show $\delta^{13}C$ compositions (-27‰ to -17‰) closer to those of organic carbon than the accepted mantle range (-4 to -8‰) (Pearson et al., 1989, 1991, 1993). Using Sr, Nd and Pb radiogenic isotopes, Varas-Reus et al. (2018) also identified an enriched mantle (EMII-type) component commonly ascribed to recycled oceanic crust with, however, different amounts of continental terrigenous sediments- recycled upper and lower continental crust. They concluded that the Sr-Nd-Hf isotopic compositions and old Re-Os model ages of Beni Bousera garnet graphite clinopyroxenites (Kumar et al., 1996) support their derivation from ancient (1.5–3.5 Ga) oceanic crust recycled along with continental crusts sediments and intimately stirred with peridotites by convection. However, Varas Reus et al. (2018) challenged the interpretation of diamondiferous garnet pyroxenites as being high-pressure cumulates. Although their primary mineral assemblage was dominated by garnet and aluminous pyroxenes, these rocks display silica-undersaturated bulk-rock compositions excluding sources such as MORB-like eclogites, oceanic gabbros and troctolites, as well as partial melts or residues of small degrees of partial melting of such sources that also are silica-saturated. Varas Reus et al. (2018) suggested that group-B pyroxenites were rutile-bearing, garnet-dominated restites formed after partial melting of recycled olivine-rich oceanic cumulates or bodies of subducted oceanic crust hybridized with mantle peridotites during stretching and stirring in the convective mantle, in addition to small amount of rocks from the garnet-rich lower continental crust. In that model, common Group-C pyroxenites that have intermediate compositions between Group-A and Group-B garnet pyroxenites most likely have sampled hybrid protoliths (Varas-Reus et al., 2018).

Late magmatic events have obliterated the original depletion in Large Ion Lithophile Elements (LILE and Light Rare Earth Element –LREE) of the three groups of garnet pyroxenites (Gysii et al., 2011 ; El Atrassi et al., 2014 ; Varas-Reus et al., 2018). Garnet websterites record interactions with LREE-rich alkali silicate melt before the uplift of the massif within crustal formation, yielding to accessory hydrous phases (intergranular subhedral kaersutite and less abundant Ti-phlogopite ; El Atrassi et al., 2014). Garnet clinopyroxenites show disseminated Ti-pargasite and

plagioclase crystallized from a LREE-depleted silicate melt resulting from partial melting of a garnet-bearing source similar to the garnet pyroxenites from the Beni Bousera massif (El Atrassi et al., 2014). These metasomatic events were ascribed to a late heating event at T below ca. 1050°C for a depth of at least 30-40 km (El Atrassi et al., 2013, 2014 ; see also Kornprobst et al., 1990 ; Gysi et al., 2011). Evidence of in-situ partial melting in Group-B garnet clinopyroxenites are provided by micrometer sized silicate films intercalated between graphite flakes (El Atrassi et al., 2011, 2013, 2014). The events of partial melting, late heating and metasomatism are closely related to the late Oligocene exhumation of mantle rocks as a thinned subscontinental lithosphere, in agreement with radiogenic isotope pairs of lithophile elements (Lu-Hf; Sm-Nd) that yield ages ranging between 24.1 ± 8.6 Ma (Lu-Hf) and 20.9 ± 4.0 Ma (Nd-Sm) (Pearson & Nowell, 2004; Blichert-Toft et al., 1999).

PETROGRAPHIC NOTES

Eight garnet pyroxenite samples were selected for this study, all coming from the ariegite subfacies in the southern western part of the Beni Bousera massif, near the wadi Ljouj (Fig. 1). Samples 3108, 2308 and 3308 were previously documented by El Atrassi et al. (2011, 2013). These are group-B graphite garnet clinopyroxenites sampled from the core and the rims of a 2 m-thick layer. The other five samples (3408, 3208, 11PY, 3008 and 2008) collected for this project are “common”, group-C graphite-free garnet clinopyroxenites. All of these samples show foliated porphyroclastic microstructure which somewhat obscures their primary mineralogy (Fig. 2a). Millimeter-sized primary clinopyroxene (Cpx1) and garnet (Gt1) porphyroclasts with irregular grain boundaries and embayments are embedded in a fine-grained recrystallized matrix. Clinopyroxene porphyroclasts display parallel exsolution lamellae of orthopyroxene (up to 50 vol. % in garnet websterite 3008) and secondary garnet. Garnet porphyroclasts occasionally contain inclusions of clinopyroxene, orthopyroxene and/or rutile rods. Most of the garnets developed a corona of symplectites (plagioclase, orthopyroxene, spinel, occasional clinopyroxene) which replace almost completely the garnet in garnet websterite 3008. The medium-grained matrix (200-500 μm) is composed of

recrystallized clinopyroxene, garnet dispersed within the folation plane along with green spinel, Ti-pargasite, plagioclase and ilmenite as accessory minerals. Coarse Ti-pargasite and plagioclase are present as interstitial phases along pyroxene and garnet grain boundaries and at triple junctions between pyroxenes and garnet. Ilmenite, sometimes associated with rutile, is common accessory intergranular mineral (Conquéré and Kornprobst, 1972; Lorand 1983) although it occurs in variable modal abundances from almost nothing (a few tens of grains less than 20 micrometer across per standard polished thick section of samples 3308, 2008 and 3208) to abundance levels of major minerals (hundreds of individual grains, up to 400 μm across in samples 3108 and 3008)(Table 1).

There is a consensus that these massifs show an extended petrological record from early exhumation at the roots of a thick continental lithosphere in the diamond stability facies (>4.5 GPa, e.g. Gysi et al., 2011 ; Afiri et al., 2011 ; El Atrassi et al., 2013 ; Frets et al., 2014). By combining petrological and geochemical constraints, El Atrassi et al. (2013) suggested the Pressure-Temperature path of Fig. 3 for Beni Bousera garnet pyroxenites. Initially, the pyroxenites containing graphite pseudomorphs after diamond originated at P > 4.5 GPa (stage I), likely as melting residues from a subducted melange of oceanic cumulates + continental crust sediments as concluded by Varas Reus et al. (2018). Entrained within the convective asthenosphere, the Beni Bousera mantle piece rose along an adiabatic-like gradient down to a temperature of ca. 1200°C or more which probably led to diamond graphitization (Stage II, Fig. 3). Common garnet clinopyroxenites intruded or infiltrated the peridotites at polybaric conditions during stage II (see Gysi et al., 2011). The change in cooling regime from adiabatic to conducive regime (interpreted as the base of the lithosphere by El Atrassi et al., 2013) occured at around 1200°C (or more) at a depth of 80-100 km. Cooling in the lithospheric mantle led to clinopyroxene porphyroclasts decomposition into secondary exsolution of Cpx and Opx (Stage III). The P-T conditions of stage III (1050°C ; 2P), close to the transition from garnet to spinel peridotite correspond to blocking temperature of Fe-Mg exchange between orthopyroxene and garnet (El Atrassi et al., 2013). Cooling followed a high apparent geotherm which characterizes regions with young and hot lithosphere (e.g., context of lithospheric thinning). At a temperature of around 900-

950°C and ca. 1.5 Gpa, the exsolved clinopyroxene reacted to form subsolidus garnet (Stage IV in the Ariegite subfacies). Garnet was replaced by symplectite intergrowths at around 800-850°C for P < 1 GPa (Gysi et al., 2011; El Atrassi et al., 2011; Stage V). The late reheating event (Stage VI) occurred at conditions of the transition between the Ariegite and the Seiland subfacies where it reached maximum temperature of c.a. 1050°C before incorporation of the Beni Bousera massif within high-grade granulitic country rocks (El Atrassi et al., 2014).

ANALYTICAL METHODS

Base metal sulphides (BMS) were studied on polished thick section using reflected light microscopy and scanning electron microscope-(SEM), and were analysed with electron microprobe (EMP) and laser-ablation inductively-coupled mass spectrometry (LA-ICPMS). BMS modal abundances were calculated from the bulk sulfur contents obtained at the Institut de Physique du Globe, Paris using the procedure described in detail in Labidi et al. (2012). Briefly, sulphur is extracted as H_2S from the rock powder by HCl-HF in a nitrogen flux and precipitated as silver sulfides. In the presence of Cr^{2+} ions, this method allows both acid volatile sulfides (AVS) and chromium reducible sulfides (CRS) to be quantitatively recovered. Bulk rock copper contents were analysed with solution ICPMS. BMS were analyzed with the Camparis SX 100 Cameca electron microprobe (EMP), using 15 kV accelerating voltage and 20 nA as sample current. Sulfur was calibrated using natural pyrite, Zn using sphalerite, and Fe, Ni, Cu, Co, As using pure metals. Five polished sections of GP (3208, 2008, 3008) and GGP (3308-2308) were studied in more detail using a Tescan VEGA II LSU Scanning Electron Microscope (SEM) operating in conventional (high-vacuum) back scattered electron (BSE) mode, and equipped with an SD3 (Bruker) EDS detector (Muséum National d'Histoire Naturelle, Paris, France, MNHN).

Chalcogen (Se), semi metals (As, Sb, Bi, Te) and other chalcophile and siderophile trace element concentrations (Co, Ni, Cu, Zn, Ga, Mo, Ag, Pd, Cd, In, Sn, Os, Ir, Pt, Au, Tl, Pb) were determined using laser-ablation inductively coupled plasma mass spectrometry (LA-ICP-MS) at the «Laboratoire

de Planétologie et Géodynamique, University of Nantes». The BMS phases were ablated and elements collected using a Photon Machine Analyte G2 equipped with an excimer laser (193 nm laser wavelength) and a dual volume sample cell that keeps the sample volume small and constant. Most analyses were performed with a repetition rate of 10 Hz in spot mode using a laser output energy of 90 mJ with a 50% attenuator and 20x demagnification, resulting in low fluences on the sample (<4 J/m2), to minimize pyrrhotite melting and related trace-element fractionation (Wohlgemuth-Ueberwasser et al., 2007). The ablated BMS material was transported in a mixture of H-He-Ar through a cross-flow nebulizer to a Varian 880 quadrupole ICP-MS. Given the unusually large grain size of pyrrrhotite grains, spot sizes for analyses of standards and BMS were set up to 75 μm.

The following isotopes were collected ^{34}S, ^{51}V, ^{57}Fe, ^{59}Co, ^{60}Ni, ^{61}Ni, ^{63}Cu, ^{65}Cu, ^{66}Zn, ^{69}Ga, ^{71}Ga, ^{75}As, ^{77}Se, ^{95}Mo, ^{105}Pd, ^{106}Pd, ^{107}Ag, ^{108}Pd, ^{111}Cd, ^{115}In, ^{118}Sn, ^{120}Sn, ^{121}Sb, ^{125}Te, ^{126}Te, ^{189}Os, ^{190}Os, ^{191}Ir, ^{193}Ir, ^{194}Pt, ^{195}Pt, ^{197}Au, ^{202}Hg, ^{205}Tl, ^{207}Pb, ^{208}Pb and ^{209}Bi. Possible contamination from matrix silicates were detected by monitoring the signals for Si. Isotopes of each element to be analyzed, length of analysis (for spots) and dwell time were set to minimize potential interferences and maximize counting statistics – with overall mass sweep time kept to ~1 s. Major elements (S, Fe) were counted in the low-count rate mode to avoid saturation of detectors. Palladium was analysed using the isotope ^{108}Pd to avoid the interference between $^{65}Cu^{40}Ar$ and ^{105}Pd that can be produced by co-ablated Ni- and Cu-rich phases.

A total of 78 spot analyses are available. Data were acquired in two separate 8-hours analytical sessions. For each analysis, the gas blank (laser off) was collected for 30/40 s prior and after laser ablation. Each ablation run was analyzed in detail in time-resolved count diagrams to retrieve any metal-rich microparticles not residing inside the Cu-Fe-Ni sulphides. Data reduction was done using GlitterTM software (Griffin et al., 2008). External calibration was performed with synthetic standards MASS-1 (pressed Zn sulphide powder; Wilson et al., 2002), NIST-610 glass and an in-house PGE-doped synthetic NiS (SARM-7 10; Lorand et al., 2018). Each standard was analyzed twice every ten analyses to bracket sample measurements at the beginning and at the end of a single ablation run to

reduce the effects of possible standard heterogeneity. Analyses of pyrrhotite were quantified with S as internal standard, using troilite ideal S concentration (36.55 wt.%) as indicated by electron microprobe analyses (see below); the S concentrations were corrected from Ni/S and Cu/S ratios where pentlandite and chalcopyrite were co-ablated. The detection limits in each quantification were calculated for each analysis from the gas blank and the sensitivity of the reference materials following the equations of Longerich et al. (1996). The accuracy and precision of analyses of external standards measured as unknowns (SARM-7 10 and MASS-1) are reported in Table S1 and S2.

RESULTS

Mineralogy of BMS

The BMS modal abundances calculated from whole-rock S contents increase from 0.3-0.6 wt.% in garnet pyroxenites to 0.8-1.5 wt.% in graphite garnet clinopyroxenites (Table 1). Both pyroxenite groups share many features with respect to BMS mineralogy, BMS distribution and textural relationships between BMS and other minerals. Primary, droplet-shaped BMS inclusions in clinopyroxene and garnet porphyroclasts as described in pyroxenite xenoliths (Peterson and Francis, 1977; Andersen et al., 1987; Shaw, 1997; De Waal and Calk, 1975; Sen et al., 2010) or orogenic pyroxenites (Lorand, 1989a,b) are lacking. Intergranular BMS blebs consist in quadrangular to polyhedral grains with convex-inward grain boundaries. Such grains generally occur along grains boundaries of clinopyroxene and garnet porphyroclasts (Fig. 2b,c). Some BMS grains may fill up the spaces between opx exsolution and host cpx. Garnet porphyroclasts may include several polyhedral BMS grains looking like those sited at intergranular spaces (Fig. 2c). The recrystallized matrix shows abundant flat BMS grains concordant to the foliation plane (Fig. 2d). A very small percentage (<5%) of the BMS grains detected in the studied pyroxenites are in touch with ilmenite, even in samples 3008 and 3108 that show high content of this Fe-Ti oxide (e.g. Table 1). In those grains, the BMS is rimmed by ilmenite and/or Ti amphibole (Fig. 2e). Graphite garnet clinopyroxenites differ from garnet clinopyroxenites only by larger BMS blebs (up to 3 mm) and very scarce (one or two grains per polished thick sections) composite BMS-graphite aggregates. These latter display straight contact

between BMS and graphite, and BMS blebs penetrating inside graphite lamellae (Fig. 2f).

Pyrrhotite (Po; ideally $Fe_{1-x}S$) is by far predominant (90-95% of sulphides by volume at the hand-sample scale). It is generally monocrystalline, devoid of deformation or intergrowth textures in reflected light except in one garnet clinoyroxenite (sample 3208) which shows a two-phase sigmoidal intergrowth cross-cut by continuous exsolutions of pentlandite (Pn; ideally $Fe_{4.5}Ni_{4.5}S_9$) showing parallel edges (Fig. 4b; see below). Pentlandite usually occurs as discrete blocky bodies (rare) (Fig. 2c) and as two generations of minute exsolution flames parallel to the basal plane of pyrrhotite (Fig. 2d). The coarsest Pn exsolutions consist of well developed, several micrometer-thick flames that always nucleated on the outer margin of pyrrhotite grains, at the sulphide-silicate boundary. The second generation of pentlandite exsolution is composed of smaller (<1 micrometer), evenly scattered flames parallel to the basal plane of host Po (Fig. 2d). Chalcopyrite (Cp; ideally $CuFeS_2$) is a minor BMS, representing no more than 5% of the BMS phases in garnet pyroxenites and less than 1% in the three graphite garnet clinopyroxenites. It may occur as discrete bodies (along with mackinawite, ideally $Fe_{1+x}S$) or as small-sized exsolutions and discrete stringers inside Po. No Cp nor Pn single-phase grain has been observed.

Pyrrhotite shows incipient replacement by a greyish phase, along with opening of cleavage planes which may be sealed by Fe-oxyhydroxides (Fig. 4a). Pentlandite is rimmed by violarite (ideally $FeNi_2S_4$). Some cleaved pyrrhotites may be totally pseudomorphosed by a microgranular, S-deficient pyrite. This alteration sequence is characteristic of sulphide supergene weathering (Lorand, 1983). The grains displaying such alteration were not analysed with electron microprobe nor with LA-ICPMS.

Major elements compositions (Table 2)

Pyrrhotite major element compositions were determined in one garnet pyroxenites and two graphite garnet pyroxenites. It is a troilite (FeS) nearly devoid of Ni and Cu (<0.1 at.%) in contrast to the metal-deficient pyrrhotite compositions (Fe_9S_{10} to Fe_7S_8) usually reported to occur in mantle-derived

pyroxenites (Lorand, 1989a,b; Montanini and Tribuzio, 2010; Sen et al., 2010; Aulbach et al. 2009). Our results are consistent with previous pyrrhotite analyses performed on several garnet pyroxenites collected in the Ariegite subfacies of the Beni Bousera massif (Fig.1; Lorand, 1983). The fit between our mean composition and that of Lorand (1983) is excellent (Fig. 5; Table 2). Both compositional ranges agree well with the narrow range defined by Li and Franzen (1996) for troilite (FeS to $Fe_{0.95}S$). The two-pyrrhotite intergrowth compositions identified in one garnet pyroxenites (e.g. 3208) correspond to troilite FeS and Fe_9S_{10}, a hexagonal polymorph of pyrrhotite solid solution (Power & Fine, 1976; Fig. 5).

Chalcopyrite analyses yield atomic Cu/Fe close to 1. Pentlandite shows atomic Fe/Ni >1 and up to 2 wt. % Co, as already suggested by previous analyses of pyroxenite-hosted pentlandite (Lorand, 1983).

Metallic trace phases

Back scattered electron (BSE) imaging of five polished thick sections (three garnet pyroxenites and two graphite garnet clinopyroxenites) led to the discovery of a wide range of micrometer-sized Mo-, As-, Sb-, Pb-, Ag-, Pt- or Au-rich metallic trace phases (Table 3). Tellurides and Mo sulphides (molybdenite) were found to occur in the five polished thick sections, including garnet pyroxenites or graphite garnet clinopyroxenites. Lead telluride was observed inside garnet (2308) or as euhedral crystals on the surface of troilite in GP sample 3008 (Fig. 6a). Silver tellurides, like molybdenite, were always found to be closely associated with Po. By their elongated shape and their occurrence inside the cleavage planes of pyrrhotite (Fig. 6b), Ag tellurides (likely close to Ag_2Te in composition as suggested by EDS spectra) can be interpreted as exsolution products in GP 3208. The same is also true for the lath-shaped molybdenite inclusions identified in sample 3008 (Fig. 6c) and 3308 (Fig. 6e). Molybdenite can also occur as coarser subhedral grains at the rim of Po (sample 3008; Fig. 6d). A subhedral Pt arsenide (likely sperrylite; $PtAs_2$) was detected inside the grain boundary between troilite and molybdenite.

The other trace phases were identified outside BMS grains. These are native gold (Ag-rich PbSb sulphide and Fe arsenide in GP 3008, PbS, as well as native gold in GP 2008 and GGP 2308 (Table 3; Fig. 6f). All of these trace phases occur within highly resorbed BMS grains, or inside fracture planes of silicates, suggesting remobilisation of primary minerals.

Trace element compositions of BMS (Table S3)

LA-ICPMS in-situ analyses were performed on BMS from two garnet pyroxenite samples (3208, 3008) and the three graphite garnet clinopyroxenites (2308, 3208, 3308). These samples contain mm-sized BMS grains suitable for laser ablation analysis. Of course, many in-situ analyses are actually «bulk» in-situ analyses because the laser beam diameter is quite large compared to the grain size of the Po-Pn-Cp intergrowths. The Fe vs. Ni and Cu vs. Ni plots of Fig. 7 indicate that several analyses in sample 3208 correspond to Pn-Cp or Po-Cp mixes, as expected from the occurrence of Pn and Cp as separate blocky exsolutions(e.g. Fig. 4 a,c). One analysis (3208-9) has sampled a nearly pure Cp grain (Table S3). All of the other LA-ICPMS data correspond to nearly pure troilite phases (mean Fe contents centred on 63.5 wt.%) showing negligible contribution from pentlandite/chalcopyrite, except a few Cu-rich analyses (3108-5 ; 3108-7 ; 3308-16) that have integrated several percents of Cp and several Ni-rich analyses (3008-8 ; 3108-8 and 3108-9 ; 2308-12 ; 3308-17) that may correspond to Pn-rich areas. The least contaminated Po/Tr analyses show much lower Ni, Co and Cu contents, below detection limits of our EMP analytical procedure (50-225 µg/g Ni, 5-125 µg/g Co, and 6-40 µg/g Cu)(Table S3). In contrast, Po in sample 2308 shows higher Ni (867-965 µg/g) resulting from the very fine-scale Po-Pn intergrowths identified with the SEM.

Chalcopyrite incorporates a large proportion of chalcogens (Te) and chalcophile elements (Ag, Cd, Zn, Sn, In, Tl and Au) relative to coexisting pyrrhotite. Tellurium broadly positively correlates with Cu and Ag with Te (Fig. 8). Indium concentrations define a better correlation with Cu suggesting that In enters chalcopyrite by a coupled substitution $CuInS_2$ - $CuFeS_2$ (Fig. 8). Correlations between Se and Cu or Te and Ni (not shown) are lacking, suggesting that chalcopyrite does not preferentially

incorporate Se, while pentlandite does not show preference for Te.

Pyrrhotite analyses are available for the five pyroxenite samples selected for LA-ICPMS analyses. Selenium abundances decrease from garnet clinopyroxenite GP 3208 (42.6-53 μg/g) to the other samples analysed (18.6-33.15 μg/g in sample 3008; 11-38.27 μg/g in sample 3108, 14.56-30.3 in sample 2308 and 18.8-38.5 μg/g in sample 3308; Figs. 9, 10). Note that Po and Cp display similar Se concentrations in sample 3208, thus suggesting a partition coefficient of 1 between the two phases (Table S3). Due to decreasing Se concentrations, S/Se increases from 6,500-8,690 for 3208 Po (idem for Cp) to 9,125-36,500 in the other samples analysed, far above the primitive mantle values of c.a. 3,000 (Lorand & Alard, 2010; Wang & Becker, 2013).

Pyrrhotites are depleted in Te (0.2-2.72 μg/g) (Table S3). In-situ measured Se/Te ratios range from 10 to 100, with most data clustering between 10 and 50 (Fig. 9B). Actually, this ratio shows great variability at the hand sample scale, likely reflecting both the heterogeneous distribution of chalcopyrite, the main Te carrier in sample 3208, and the evenly distributed Te-rich trace phases (lead and silver tellurides) that were identified with the SEM. Beni Bousera garnet pyroxenites show strong depletion in the other chalcogens (As, Bi and Sb). Apart from a Bi (1-4 μg/g) and Sb enrichment in 2308, these elements occur at low concentrations levels, close to limits of detection for As and Sb (Fig. 10). The As concentration peaks detected in sample 3008-2 (up to 29 μg/g) correlates to Pb, Te, Ag, Pt which may indicate that a complex telluride + arsenide was integrated by the LA-ICPMS analysis (Table S3). The pyrrhotite displays positive Mo and Bi anomalies in the three graphite garnet clinopyroxenites (up to 25 μg/g Mo in some pyrrhotite analyses of sample 2308). Molybdenum broadly covaries with Tl (Fig. 11). Like Te, erratic variations of Mo concentrations (e.g . samples 2308 and 3208) likely result from molybdenite microparticles.

Palladium and other highly siderophile elements (HSE: Os, Ir, Pt, Pd, Au) are uniformly *depleted,* in concentrations often below limits of detection, especially Ir, Pt and Au (<0.05 μg/g) compared to the other trace elements measured with LA-ICPMS. Previous analyses of mantle pyroxenitic BMS reported HSE concentrations one order of magnitude higher (Luguet et al., 2008; Van Hacken et al.,

2010; Sen et al., 2010). Only Pd preferentially partitions in Pn, as suggested by coupled increase in Pd and Ni concentrations (not shown).

Moderately chalcophile elements V, Ga and Zn correlate *two by two* (not shown) which likely indicates contamination of the LA-ICPMS analyses by Fe-Ti oxides (Lorand et al, 2018), especially abundant in garnet websterite 3008 (half of the analysed grains; Table S3).

DISCUSSION

Cooling history of BMS

The combination of pyrrhotite with minor pentlandite and chalcopyrite is typical of primary BMS assemblages of magmatic rocks, whether basalts (e.g. Craig & Kullerud, 1969 ; Czamanske & Moore, 1977 ; Patten et al., 2012), gabbros (e.g. Puchtel et al., 1996), mantle-derived pyroxenites (Andersen et al., 1987; Shaw, 1997; Lorand, 1989 a,b; Sen et al., 2010; Montanini et al., 2010), as well as mafic granulites (Kawakami et al., 2006) and eclogites (Aulbach et al. 2009 ; Gréau et al., 2013). The covariation trend between BMS modal abundances and graphite occurrence indicate that both phases share the same origin in Beni Bousera garnet pyroxenites. It is concluded that BMS existed as early as Stage 1 in the P-T path of Fig. 3 and recrystallized along with graphite on retrogession from the diamond (Stage 2; Fig. 3). Our conclusion is supported by observation of BMS blebs intercalated within graphite lamellae (Fig. 2f). Experiments on troilite by Rhyzenkho & Kennedy (1973), Palyanov et al. (2007) and Bataleva et al. (2019) suggest that the BMS phase was solid in the diamond stability field and remained so during Stage 2 adiabatic cooling (Fig 3). However, the BMS grains of Fig. 2 combine the polygonal shape with convex-inward grain boundaries, as expected for solidification products of immiscible sulphide melts trapped in the interstitial pores of silicate rocks (Wang et al., 2020 and reference therein). Sulphide (re)melting during Stage 2 is not excluded because the adiabatic cooling path is located very close to the liquidus curve of troilite in Fig. 3.

A basic prerequisite for a more complete assessment of the crystallization/exsolution history

of BMS is to recalculate the bulk composition of BMS assemblages for each of the five samples analyzed. This was done by averaging the in-situ LA-ICPMS analyses for the five samples studied (Table 4). The bulk-rock Cu/S ratios were used to correct the Cu contents in 100 wt.% BMS and then the Cp weight fraction assuming that Cu is mostly accommodated in BMS (Lorand & Luguet, 2016). The available LA-ICPMS analyses of chalcopyrite were integrated to the bulk BMS composition taking into account chalcopyrite/pyrrhotite modal proportions (normalized to 100 wt. BMS) as estimated from the bulk-rock Cu/S ratio. The bulk Ni data reported Table 4 were obtained by averaging the LA-ICPMS analyses with integration of the few analyses that intercepted discrete Pn grains.

In the ternary Fe–Ni–S system at 1 atm pressure and 1100°C (Fig. 12), the bulk compositions of Beni Bousera garnet pyroxenites plot close to the FeS end of the monosulfide solid solution (mss) field, the high-T precursor of low-T pyrrhotite phases (see next section). On average, our composition plot at lower Ni and Cu concentration level compared to previous analyses of mantle-derived pyroxenitic BMS. According to experiments in the Cu-Fe-S system and analyses of quenched basalts, mss can accomodate up to 7 wt.% Cu at 935°C (Craig & Kullerud, 1969 ; Ballhaus et al., 2001; Helmy & Fonseca, 2017) and still ca 1 wt. % Cu at T< 600°C (Czamanske & Moore, 1977; Mc Queen, 1979 ; Fleet, 2006; Patten et al., 2012). This means that chalcopyrite exsolved from the mss at T <600°C in Beni Bousera garnet pyroxenites, in line with its occurrence as stringers and blebs inside pyrrhotite. Likewise, the troilite-pyrrhotite phases are nearly devoid of Ni while containing abundant pentlandite exsolution flames. Kelly & Vaughan (1983) and Etschmann et al. (2004) experimentally documented pentlandite flames similar to the smallest flames evenly distributed inside the pyrrhotite as formed at T<100°C by homogeneous nucleation from the last batches of Ni still held in solid solution by Po phases at such temperatures. This temperature of final reequiibration is supported by the intergrowth of troilite and metal-deficient pyrrhotite (47.8 at.% Fe) analysed in sample 3208. Such intergrowth formed by subsolidus decomposition of Po/mss (disordered 1C hexagonal structure ; C = c parameter of NiAs subcell in Nakazawa and Morimoto (1971) nomenclature of

pyrrhotite phases). This high temperature phase undergoes a phase transition at T = 100 to 140 °C, yielding to co-crystallization of troilite and hexagonal pyrrhotite (Fe_9S_{10}) (5C structure in Nakazawa and Morimoto (1971) nomenclature) below 100°C (Fig. 5).

A slightly different scenario can be proposed for the cooling of sample 3208 that shows coarse-grained bodies of pentlandite and chalcopyrite in addition to thin, micron-sized flames inside the pyrrhotite. Such bodies may be interpreted as crystallization products from a Cu-Ni-rich sulphide melt residual after crystallization of mss, as postulated for similar sulphide occurrences in mafic/ultramafic rocks (e.g. De Waal & Calk, 1975; Czamanske & Moore, 1977; Patten et al., 2012; Lorand & Luguet, 2016; Mansur and Barnes, 2020 and references therein). Peregoedova et al. (2004) experimentally produced a Cu-rich sulphide melt by desulfidation of mss at 1,000°C. Experiments in the Cu-Fe-Ni-S system indicate that this sulphide melt crystallizes as a high-T (875°C) coarse-grained pentlandite coexisting with the mss and then, a Cu-rich Intermediate Solid Solution (Iss) at 550°C, the precursor of chalcopyrite (Fleet, 2006 ; Kitakaze et al., 2016 and references therein). Since the sulphide melt incorporates high abundances of metalloids (e.g. Te, Bi, As) and metals (Cu, Ag, In etc) (Liu & Brenan, 2015; Helmy et al., 2010; Wohlgemuth et al., 2010; Mansur & Barnes, 2020), high-temperature Pn and Cp like those observed in GP 3208 are enriched in those elements. In contrast to Te, the chalcogen Se almost equally partitions between mss and sulphide melt (Wohlgemuth-Uberwasser et al., 2010; Liu & Brenan, 2015; Helmy & Fonseca, 2017), which explains its equal distribution between Po, Pn and Cp in sample 3208 (Table S3).

Strongly reducing conditions during subsolidus cooling of BMS assemblages.

It can be deduced from the crystallization sequence discussed above that BMS were solidified within the mantle (Stages 4-5-6 ; Fig. 3). Subsolidus decomposition reactions obviously took place during the crustal uplift and went close to completion at near surface temperatures. This sequence of event occurred under specific redox conditions compared to mantle-derived pyroxenites documented so far for BMS. The common metal deficiency nature of pyrrhotite is ascribed to iron atoms existing in both

states of Fe^{2+} and Fe^{3+} (hole state), the charge excess resulting from trivalent iron being balanced by vacancies in the metal sublattice of pyrrhotite (e.g., Power & Fine 1976; Wang & Salveson, 2005 and references therein). Pyrrhotite compositions are therefore a qualitative sensor of both sulfur and oxygen fugacity (Hall, 1986; Pasteris, 1985; Eggler & Lorand, 1993). In nature, troilite is not as abundant as the more metal-deficient pyrrhotite minerals because it forms under strongly reducing conditions (e.g. Pedersen, 1979). At P = 1bar, troilite is stable with graphite and native iron which places the fO_2 slightly above the iron-wustite (IW) equilibrium for Beni Bousera pyroxenitic BMS that are devoid of metallic iron (Fig. 13). Increasing pressure expands the stability field of elementary carbon : at 150 km (5 GPa), it is stable as diamond to slighly higher fO_2 conditions equivalent to IW+2.5-3 log unit (Fig. 13; Ulmer & Luth, 1991; Frost & Wood, 1997; Stagno & Fei, 2020 and references therein). For these P-fO_2 conditions, a slightly metal-deficient pyrrhotite (M/S = 0.99, i.e. Fe atomic percent = 49.5) is expected to be stable along with elementary carbon and magnetite if elementary carbon buffers fO_2. However, this shift in pyrrhotite composition remains within the analytical errors of the electron microprobe analyses and too small compared to the spread in troilite analyses of Fig. 5. One may therefore speculate that the uplift from the diamond stability field (Stages II to VI; Fig. 3) did not alter significantly the primitive fO_2 conditions recorded by BMS. Troilite compositions does not seem to be linked with graphite occurrences : whether graphite-bearing or not, all garnet pyroxenites from the Ariegite subfacies of the Beni Bousera massif show homogeneous troilite compositions (Figs. 1, 5). The metal-deficient pyrrhotite composition analysed in a graphite-free garnet pyroxenite (3208) is very scarce and could represent local conditions enhancing subsolidus decomposition of 1C pyrrhotite (Fig. 5). Despite being graphite-bearing, Eastern Ligurian garnet pyroxenites exhumed from ca 90 km preserve strongly metal-deficient pyrrhotites (M/S = 0.94-0.85 ; Montanini et al., 2010) indicating more oxidizing conditions, as do other mantle-derived garnet pyroxenites devoid of graphite (Lorand, 1989a,b ; Sen et al., 2010). The same is also true for diamond-hosted BMS inclusions of eclogitic affinity exhumed from similar depths as our Beni Bousera graphite garnet pyroxenites (see below). To summarize, Beni Bousera

garnet pyroxenites likely inherited their strongly reducing conditions primarily from their mantle source, before or during stage I. A significant change of their pyrrhotite compositions during uplift is excluded.

Metallic trace phases as exsolution products from subsolidus cooling of BMS.

Metallic trace phases (Pb and Ag tellurides; molybdenite), are likely subsolidus exsolution products from the mss/pyrrhotite phases as they commonly occur inside or in the immediate vicinity of pyrrhotite phases. Heavy metals (Ag, Pb) and the semi-metals Te, As, Bi, Sb are large-sized chalcophile elements showing low preference for regular octaedral sites and thus create distorsion in the mss lattice. Tellurium is less compatible in mss than Se and S due to its greater ionic radius (Te^{2-} = 2.11 Å vs. 1.88–1.90 Å for Se^{2-} and 1.56–1.78 Å for S^{2-}). Therefore, Te will commonly tend to form tellurides during later stages of subsolidus cooling. However, although showing much higher preference for Cu-Ni sulphide melt, these elements can be incorporated in the mss lattice at high temperatures (>1,000°C) (Helmy et al., 2010 ; Li &Audetat, 2012, 2015 ; Liu & Brenan, 2015), As pointed out for pyrite, the Gibbs-free energy of mixing becomes increasingly more negative at higher temperatures allowing the lattice structure to tolerate higher concentrations of Se and Te (Maslennikov *et al.*, 2009). being enhanced by lattice metal vacancies (e.g., Ballhaus & Ulmer, 1995; Helmy et al., 2010). Thus, extensive subsolidus decomposition of mss on cooling and the strongly reducing conditions precluding vacancies in the metal sublattice of the pyrrhotite, likely enhanced the exsolution trace metals and semi metals with large ionic radius such as Ag, Te, Pb, Mo. Lead and Ag tellurides are common accessory minerals in epithermal (<300°C) hydrothermal orebodies (e.g. Hedenquist & Arribas, 2000; Pals & Spry, 2003). Silver tellurides are stable at T<460°C for $Ag_{5-x}Te_2$ (stützite) and 960°C for hessite Ag_2Te (Cabri, 1965 ; Ksanda et al., 1966 ; Karakaya & Thomson, 1991). The low fTe_2 necessary to precipitate hessite explains the common occurrence of this telluride in Te-poor systems (Afifi et al., 1988). A better assessment of silver telluride mineralogy would nevertheless require further analyses as the EDS spectra collected during SEM analyses cannot

discriminate the two phases stützite and hessite. Unlike Te, Se readily substitutes for sulfur in BMS minerals (e.g. Simon et al., 1997 ; Lorand & Alard, 2010 ; Queffurus & Barnes, 2015; Helmy & Fonseca, 2017). Our data confirm the view that Se substitutes for S in mss and does not form discrete selenide phase in mantle-derived pyroxenites, being therefore decoupled from Te during subsolidus cooling experiments.

The widespread occurrence of molybdenite microinclusions in pyrrhotite is another key feature of Beni Bousera garnet pyroxenites. Although the atomic radius of Mo is significantly different from Fe and S (e.g., Large et al., 2017), this element can enter the mss structure at magmatic temperatures : Mengason et al. (2011) found 1140-1470 µg/g Mo at 1bar pressure, 1042°C and fO_2 at the Ni–NiO oxygen fugacity buffer in a metal-deficient mss (Fe/S = 0.9-0.95) ($D_{Mo}^{\text{mss-silicate melt}}$ = 35±3 ; $D_{Mo}^{\text{mss-sulphide melt}}$ = 90 ±10). $D_{Mo}^{\text{mss-sil melt}}$ was shown by Mengason et al. (2011) to increase with decreasing fO_2, and with increasing fS_2, reaching significantly higher values (e.g., > 1000), in the magnetite-free pyrrhotite-only stability field. Li & Audétat, (2012) confirmed the greater preference of Mo for mss ($D_{Mo}^{\text{mss-sulphide melt}}$ > 10) at reducing conditions (IW + 2 log units), 1175-1300°C and 1.5-3.0 GPa, compared to Te, for example. They experimentally determined Mo concentrations at several orders of magnitude higher than those measured in Beni Bousera pyrrhotites, a feature suggesting that molybdenite exsolved at the end of the subsolidus cooling, yet at an unknow temperature. The fact that molybdenite may occur as external grains over pyrrhotite grain boundaries as well as tiny exsolution flames inside pyrrhotite suggests a temperature-driven continous exsolution process: by analogy with pentlandite exsolutions in pyrrhotite (e.g. Kelly & Vaughan, 1983 ; Etschmann et al., 2004), one may infer that the coarsest external grains (requiring long-range diffusion of Mo within Po) exsolved at higher temperature than lamelar exsolutions that involved in-situ nucleation and short-range diffusion of Mo.

Origin of BMS in graphite garnet clinopyroxenites by two-component mixing.

Evidence for recycled sedimentary component.

The concomitant occurrence of BMS and elemental C indicates that graphite garnet clinopyroxenites received a significant part of their S budget and associated chalcophile siderophile metals contents from the crustal component that also delivered C before Stage I (Fig. 3). By the same way, this relationship excludes any significant input of S from the metasomatic event(s) postdating graphite formation, namely by the small melt fractions that precipitated metasomatic Fe-Ti oxides and Ti-rich hydrous silicates (pargasite, phlogopite) during the late-stage reheating coeval with the Oligocene emplacement of the Beni Bousera massif (Stage VI in Fig. 3). These latter did not produce covariation trend between BMS modal abundance and Fe-Ti oxide modal abundance, thus excluding significant remobilization of BMS during stage VI. The few composite BMS-FeTi oxide grains observed show textural relationships supporting nucleation of metasomatic phases (amphibole, ilmenite) over preexisting BMS, and not the opposite (e.g. Fig. 2e).

According to lithophile trace element geochemistry and stable isotopes (O, C)(Pearson et al., 1991; 1993), Beni Bousera garnet pyroxenites tapped an altered oceanic crust that incorporated 2-5 wt.% terrigeneous sediments of continental crust origin (Varas Reus et al., 2018). The very ^{13}C-depleted carbon isotopic composition determined for the graphite pseudomorphs (-27‰<$\delta^{13}C$<-17‰) supports a biogenic provenance for C (Pearson et al., 1989, 1991). Carbon-rich reduced sediments such as black shales can bring both S and C under the reducing conditions (close to IW) required by the troilite compositions of Beni Bousera samples. Both components, i.e. MORB-type oceanic crust and reduced sedimentary lithologies can be identified through Fig. 14 which display the mean bulk BMS compositions calculated for the five Beni Bousera samples studied. Their patterns more or less mimic the pattern of MORB-hosted BMS published by Patten et al. (2013), with, however, a systematic depletion in all chalcophile-siderophile elements but Mo (Fig. 14). Compared to MORB-hosted BMS, Beni Bousera pyroxenitic BMS show more fractionated S/Se (7,872-19,776), well within the superchondritic range published for sulfidic black shales (5,000 <S/Se< 38,000; mean = 18,710) (e.g. Queffurus & Barnes, 2015 ; Samalens et al, 2017 ; Layton Mathews et al., 2013). Black shales also display Se/Te (10-50) within the range of Beni Bousera garnet pyroxenites (15-31;

Schirmer et al., 2014; Samalens et al., 2017; Parnell et al., 2018), bearing in mind, however, that the bulk Te contents of Beni Bousera BMS were probably underestimated by the occurrence of widespread discrete telluride microphases that may or may not be intercepted by the laser beam.

Organic-rich shales commonly display metal and metalloïd enrichment, absorbed by organic matter during sedimentation in strongly anoxic environments (Coveney & Glascock, 1983; Coveney & Martin, 1983; Patterson et al., 1986; Crusius et al., 1996; Algeo & Maynard, 2004; Rimmer, 2004). Selenium (like Bi) is typically concentrated by organic processes during sedimentation in strongly anoxic environments (Yierpan et al., 2020 and references therein). Molybdenum contents of BB pyroxenitic BMS, coupled with their widespread molybdenite microinclusions also support a black shale contribution. In reducing sediments, Mo contents characteristically correlate with the organic carbon content (Algeo & Maynard, 2004). Extreme Mo enrichments up to 1,160 µg/g, coupled with Se- (250 µg/g), Cu- (420 µg/g) and Ni- (450 µg/g) enrichments, were reported in Pensylvanian black shales (e.g. Coveney & Martin, 1983 ; Rimmer, 2004). Molybdenum concentrates first by forming thiomolybdate complexes in euxinic (S-rich) waters, then this element partitions into early synsedimentary pyrite that captures Mo as Mo-Fe-S cuboidal clusters during diagenesis (Coveney & Martin, 1983 ; Helz et al., 1996 ; Erickson & Helz, 2000 ; Gregory et al., 2015a,b ; Shawar et al., 2018).

How much S in the bulk rock analyses of Table 1 comes from the putative recycled sedimentary contaminant can be estimated using the crust/sediments ratios (98/2 to 95/5) estimated by Pearson et al. (1989; 1991) and assuming a conservative S content of 1,000 µg/g in the oceanic crust rocks [Alt, 1995]). The result (4,000 ± 1,000 µg/g S) corresponds to a sedimentary component containing at least 100,000 µg/g S (10 wt% S) as reported for sulfidic black shales (Rimmer, 2004; Schulze, 2004 ; Cruse et al., 2004). Published bulk-rock metal/S ratios for sulfidic shales can be used to recompute some chalcophile and siderophile metal contents of Beni Bousera graphite garnet pyroxenites. The Mo/S ratio (0.002-0.004) yields 45(±20) µg/g Mo, well within the values documented for sample 2308. The BMS composition expected by mixing mantle-derived MORB

BMS (Patten et al., 2013) and black shale pyrite (Gregory et al., 2015 ; 2019) has been semi-quantitatively modelled taking respective inputs of 80±10% by weight of pyrites and 20±10% MORB-hosted BMS, as dictated by the bulk-rock S contents of garnet graphite clinopyroxenites (Table 5). The fit is rather good for Os, Ir, Se and to a lesser extent Mo while Te, Ag, Pb and Mo concentrations are underestimated in our model, likely because these metals occur as trace phases in Beni Bousera BMS that may generate sampling bias during LA-ICPMS analyses (Fig. 14). Our measured concentrations for Ni, Au, and Cu may reflect the diluting effect of the sedimentary component on MORB sulphides. This is suggested by the composition of metamorphosed black shale country rocks (Basal Pyrrhotite Unit-BPU; Samalens et al., 2017) of the Duluth layered intrusion (Minnesota, USA). As pointed out above concerning Highly Siderophile Eelements (HSE), the bulk composition of Beni Bousera BMS is significantly depleted in line with the scarcity of platinum-group minerals, especially Pt- and Pd-tellurides that are widespread in pristine mantle rock (Lorand & Luguet, 2016 and references therein). The balance for these elements is not straightforward to assess because in-situ analyses of these elements in black shale pyrite are quite rare and produced highly variable results. Our calculation does not contradict a black shale contribution for HSE too if it is based on Gadd et al. (2019) data for Canadian (0.05-0.1 μg/g Pt, Pd, Au in framboïd matrix pyrite) and Chinese black shales deposits (0.10 μg/g Pt, 0.11 μg/g Re and 1.40 μg/g Au ; Ru, Rh, Pd, Os and Ir were below detection limits of <0.05 μg/g for 144 analyses).

Subduction-related modification of fluid-mobile trace element contents

Our BMS bulk-compositions are variably depleted in the semi-metals (Te, As, Sb, Bi) compared to black shale compositions (taken as mean pyrite compositions of Gregory et al. (2019)) or the BPU unit of Samalens et al. (2017) (Fig. 14). As suggested above, the Te depletion may reflect undersampling of discrete telluride microphases. Concerning As, Sb and Pb, all three elements are depleted by four orders of magnitude in Beni Bousera BMS ; they may have been mobilized along with Cu, Zn and Tl at various stages of the cycling of the sedimentary component in the mantle

source of Beni Bousera graphite garnet pyroxenites predating stage I (Fig. 3). These three elements are classified as highly volatile, fluid-mobile elements that may be easily mobilized by crustal fluids (Jochum & Verma, 1996; Pokrovski et al., 1996 ; Agranier et al., 2007 ; Aulbach et al., 2012 ; Ryan & Chauvel, 2014; Evans et al., 2014; Helmy & Botcharnikov, 2020 and references therein). Arc basalts display enrichments in As, Sb, Tl, Pb, and Bi that have been attributed to the influence of hydrothermally altered oceanic crust that concentrates these elements into sea-water derived hydrothermal sulphides (pyrite and/or chalcopyrite) in addition to sedimentary sulphides (Mengason et al., 2011; Jenner et al., 2012). A major contribution of hydrothermal BMS to the chalcophile/siderophile trace element composition of Beni Bousera garnet pyroxenites is however unlikely, due to the very low Cu contents of BMS. Moreover, hydrothermal BMS show much larger variation of S/Se (<1,000->100,000), mainly reflecting their highly variable Se contents (between < 1 µg/g and > 1000 µg/g Se) (Luguet et al., 2004 ; Yang & Scott, 2002 ; Layton Mathews et al., 2013).

The fate of fluid-mobile elements depends on which BMS are transferred by the subducted oceanic lithosphere. Regarding Beni Bousera pyroxenites, the precursor oceanic crust protolith of garnet pyroxenites likely entrained both minor igneous BMS (po-pn-cp), rehomogeneized as monosulphide solid solution (mss) once temperature exceeded 600°C upon subduction (see "Base metal sulphides and secondary processes during exhumation of the massif") and abundant sedimentary sulphides as pyrite. Mss can survive recycling into the mantle, as suggested by observations in ultra-high pressure rocks that preserve mss reequilibration products enclosed in garnet of eclogites (Gréau et al., 2013; Evans et al., 2014 ; Deines & Harris, 1995; Thomassot et al., 2009). The respective stability of pyrite and pyrrhotite/mss during slab burial and eclogitic metamorphism were summarized by Walter et al. (2020), who documented a strong dependence on redox conditions. Pyrite is stable under the oxidized conditions of the upper crust (nickel-nickel oxide-NNO buffer) while pyrrhotite should be preserved in the more reduced deep crust (see also Hall, 1986). In methane-bearing rocks, pyrite can decompose into pyrrhotite by releasing H_2S and producing reduced carbon at moderate temperature (<800° C ; cf Kawakami et al., 2006) according to the following reaction $CH_4 + 2\ FeS_2 = 2\ H_2S + 2$

FeS + C (Haggerty, 1986). Large et al (2012) identified the pyrite to pyrrhotite transition as an important reaction for mobilizing fluid mobile trace metals during metamorphism because pyrrhotite may not accommodate trace metals with large ionic radius (e.g. As, Pb, Bi, Mo) like the diagenetic pyrite does. Loss/remobilisation of fluid mobile trace elements may have taken place at this stage, controlled by both their mobility in released H_2S-rich fluids and their low affinity for the pyrrhotite phase. For example, the Mo concentrations measured in Beni Bousera pyrrhotites survived prograde metamorphism because this element in its reduced (+4) state is highly insoluble in hydrous fluids while being accommodated in the pyrrhotite lattice at fO_2 conditions corresponding to IW (see above). Likewise, the bulk-rock S enrichments of sediments were preserved thanks to the strongly reducing conditions which make sulfur poorly soluble in dehydration fluids (0.001-0.005 mol.% as H_2S-HS^- species, Evans et al., 2014) compared to the huge solubility of oxidized S species (sulfates, sulfites) (Walter et al., 2020 and reference therein). Our results is supported by recent work documenting highly reducing conditions also in subducted oceanic crust now sampled as both Phanerozoic orogenic eclogites (i.e. not altered during retrograde exhumation) and older eclogite xenoliths, which have been shown to be in equilibrium with CH_4-dominated fluids (Aulbach et al. 2017, 2019 ; Tao et al. 2020). These authors concluded that sulphate S does not play a significant role in S transfer by subducting oceanic crust (even where evidence of seafloor alteration is indicated by non-mantle $\delta^{18}O$ and/or variable $\delta^{18}O$ at a single locality). Further support recently came from S-isotopes in BMS from strongly subduction-modified supra-subduction zone mantle, which interacted with crustal melts (Consuma et al., 2021).

Proterozoïc partial melting and mobilisation of C and S from sedimentary sulfides

Our data are entirely consistent with a common origin for C and S in Beni Bousera graphite-garnet clinopyroxenites, i.e. organic-rich reducing terrigeneous sediments mixed with altered cumulates from recycled oceanic crust (Varas Reus et al., 2018). The event that could have ensured efficient mixing of both component inside the mantle is the Proterozoïc partial melting event that left group B pyroxenites as solid residues inside the convecting mantle before stage I (Kumar et al., 1996 ;

Pearson and Nowell, 2004 ; Varas-Reus et al., 2018). Partial melting models predict that the S fraction solubilized within the partial melt (Sulfide Content at Sulfur Saturation) will be easily extracted (e.g. Holzheid and Groves, 2002). The Sulfide Content at Sulfur Saturation cannot be estimated with great confidence without detailed information on major element composition of the hypothetical melt extracted from graphite garnet clinopyroxenites (namely its FeO content; Mathez, 1976; Bézos et al., 2005). Literature data indicate that MORB-type partial melts can dissolve ca. 800 to 1,500 μg/g S at P = 100 bars (Mathez, 1976; Bézos et al., 2005; Jenner et al., 2012 ; Lisner et al., 2014 ; Labidi & Cartigny, 2016). However, the solubility of S in mafic melts decreases significantly with increasing pressure : the model calculations of Mavrogenes and O'Neill (1999) suggest 400 μg/g S (c.a. 0.1 wt.% BMS) or less in MORB-type melts in the stability field of diamond (e.g. Sen et al., 2010). If applied to Beni Bousera graphite garnet clinopyroxenites, these estimates suggest that 10% only of the initial S budget was entrained by partial melts. The remaining fraction, ~90% of bulk S, would be featured within residual lithologies, as trapped molten BMS, as widely documented by peridotitic lithologies (Holzheid and Groves, 2002 ; Aulbach et al., 2009 ; Lorand and Luguet, 2016 and references therein).

Wang et al (2020) recently modelled the interaction between silicate melt and sulfide melt during extraction of partial melts from peridotite matrix. They showed that, under hydrostatic conditions and in the presence of low to moderate amount of silicate melt, this latter may impede the mechanical extraction of sulfide liquid through the porous flow of silicate melt due to the larger excess pressure imposed by the capillary force, low flow rates of silicate melt generating a higher percolation threshold for sulphides (5 vol.%). Most sulfide droplets (>0.3 μm) would be stranded and choked in melt junctions or pockets ; under longer timescale conditions, large sulfide droplets tend to grow until they are large enough to block the pore throat of melt channel, thereby further prohibiting the melt extraction process. This prediction is met by observations in Beni Bousera graphite garnet clinopyroxenites that show intergranular BMS with the size (mm) and modal abundances (<5 vol.%) predicted by the melt extraction model of Wang et al. (2020). Both features support their origin as the

remaining fraction retained inside porosity of residual pyroxenites. Another interesting feature supporting the residual origin postulated by Varas-Reus et al. (2018) is the absence of primary BMS inclusions in clinopyroxene and garnet porphyroclasts. Such primary BMS inclusions are common in cumulate pyroxene megacrysts from alkali basalts (Peterson & Francis, 1977; Andersen et al., 1987) and mantle pyroxenites of undisputed cumulative origin (Lorand, 1989a,b; Shaw, 1997; Sen et al., 2010). Such inclusions were interpreted as sulphide melt droplets trapped along the growing faces of cumulus silicates. Their absence from our samples is therefore better explained if type-B garnet pyroxenites are of residual origin since no magmatic growth of silicates (and concomittant trapping of BMS droplets) is expected to occur in that model. Because of their contorted shapes ressembling intergranular BMS and their occurrence with fracture planes, the BMS grains enclosed in garnet porphyroclasts (Fig. 2c) were likely trapped during solid-state recrystallization/deformations coeval with stage III to V (Fig. 3).

Most of the interpretation discussed here can be extended to Group-C graphite-free garnet websterites and clinopyroxenites that share so many features with graphite garnet clinopyroxenites as regard their BMS assemblages. These noteworthy features are i) no primary BMS inclusions in silicates, ii) intergranular BMS assemblages dominated by troilite, iii) similar chalcophile siderophile trace elements patterns coupling fractionated S/Se with Mo concentration peaks and iv) widespread molybdenite inclusions in troïlite. Such similarities are consistent with interpretation of Group-C garnet pyroxenites as derived from hybrid sources involving the same components, but in different proportions, as group-B graphite garnet clinopyroxenites (Varas Reus et al., 2018). The twice lower bulk-rock S contents of group-C garnet pyroxenites probably indicates lower contribution of organic-rich reducing sediments delivering S and C, in line with the absence of graphite.

Comparison with diamond-hosted BMS inclusions

Our database provides some clues for a comparison with the well-known BMS-diamond association. Eclogitic diamonds are characterized by the same pyrrhotite-dominated BMS inclusions with minor

chalcopyrite and pentlandite, as Beni Bousera garnet pyroxenites, except for their metal-deficient Po compositions (average (Fe + Co + Ni + Cu)/S) = 0.9±0.04) and higher bulk Ni contents (Fig. 15; e.g. Deines & Harris, 1995; Clemens et al., 2008; Thomassot et al., 2009; Aulbach et al., 2012 ; McDonald et al., 2017; Kempinnen et al., 2018). The two complete datasets for trace chalcophile/siderophile elements contents available for eclogitic diamonds are those of Aulbach et al. (2012) who analysed 28 BMS inclusions extracted from 15 eclogitic diamonds of the Lac des Gras kimberlitic field, Canada (Diavik Mine) and McDonald et al. (2017) who reported analyses of 7 BMS inclusions (Orapa; Kaapval craton, South Africa) which were rehomogeneized before LA-ICPMS analyses (Fig. 15) Compared to Beni Bousera BMS, eclogitic BMS show similar primitive-mantle normalized patterns characterized by overall depletion in both highly siderophiles (Os, Ir, Pt, Pd) and volatile chalcophiles (As, Sb, Bi, Tl, In) compared to the other siderophiles (Pd, Au, Cu, Te, Se). One may speculate that, as postulated for Beni Bousera garnet pyroxenites, the fluid-mobile element depletion (including semi-metals) occurred during prograde metamorphism/dehydration affecting the subducted oceanic lithosphere. Indeed, once encapsulated in diamonds, BMS inclusions were protected from any chemical/mineralogical alteration (Aulbach et al., 2012*).* The positive Mo anomalies was recently supported by the discovery of molybdenite in eclogitic diamonds from worlwide occurrences (the Mir kimberlite (Yakutia, Russia), Argyle (NW Australia), Orapa, Letlhakane, Damtshaa (Botswana) and Dachine (French Guiana)(Kempinnen et al., 2018). This mineralogical evidence supports the part played by Mo-enriched materials in the genesis of some sulphide inclusions in eclogitic diamonds.

Diamond-hosted sulphide inclusions however display several differences, i.e. S/Se/Te systematics much closer to MORB-type BMS (11<Se/Te<58 and 2752<S/Se<6475 in McDonald et al. (2017) vs. 8,280 in Aulbach et al. (2012). Such differences may indicate greater contribution of oceanic crust BMS in the chalcophile-siderophile element budget. Another important difference is the highly metal-deficient pyrrhotite composition of eclogitic sulphide inclusions, confirmed by their ferrimagnetic properties (Clemens et al., 2008). Eclogitic BMS inclusions carry a memory of much

more oxidizing conditions compared to Beni Bousera pyroxenitic BMS. Such conditions are predicted by models of diamond production involving interaction between oxidized carbonate-bearing subducted slabs and reduced metal-saturated mantle rocks (see reviews by Cartigny, 2005 ; Stachel & Harris, 2008; Shirey et al., 2013) or between reduced oceanic crust and oxidizing CO_2-rich fluids, if, as pointed out by Aulbach et al. (2017, 2019), the Archaean oceanic crust had highly reduced compositions, markedly below carbonate stability. Zdrokov et al. (2019) reproduced the highly metal-deficient pyrrhotite compositions in their experiments on diamond production involving carbonate melts. By contrast, taken altogether, our data suggest an unusually important contribution of reducing sedimentary component for Beni Bousera graphite-garnet clinopyroxenites, as required by their high BMS modal abundance, their strongly fractionated S/Se, their diluted Ni content, coupled with troilite composition. Moreover, there are textural evidence, such as the scarcity of composite BMS-graphite aggregates or BMS inclusion in graphite (El Atrassi et al., 2011, 2013), that BMS and diamond nucleated independently in Beni Bousera graphite-garnet clinopyroxenites, although S and C share a common origin.

CONCLUSIONS

Graphite garnet clinopyroxenites show intergranular BMS with the size (~mm) and modal abundances (<5 vol.%) predicted by the melt extraction model of Wang et al (2020). Their occurrence in intergranular pores of the rocks support their origin as the remaining sulphide fraction retained inside porosity during partial melting.

The BMS assemblages exsolved from a homogeneous monosulphide solid solution compositionally close to the FeS end-member. Subsolidus reactions continued down to T<100°C, yielding to Ni-poor troilite + pentlandite + chalcopyrite assemblages. On cooling, troilite exsolved trace metal microphases (Pb and Ag tellurides, molybdenite) that have not been reported before from mantle-derived garnet pyroxenites.

Taken as a whole, our body of data supports a common origin for carbon and sulfur. The tenfold S enrichment (up to 5550 μg/g) of graphite-garnet clinopyroxenites compared to graphite-free

pyroxenites suggests that most of their bulk-rock S budget was delivered by an extraneous sedimentary component, in agreement with petrogenetic models involving altered subducted oceanic crust + terrigeneous sediments.

Pyrite-bearing black-shales are a potential sedimentary contaminant of Beni Bousera garnet pyroxenites. This is suggested by troilite compositions indicating strongly reducing conditions slightly above the iron-wustite (IW) buffer, the widespread Mo anomalies and molybdenite exsolutions inside troilite as well as the bulk sulphide compositions showing fractionated S/Se/Te systematics compared to the mantle values (7,872<S/Se<19,776 ; 15<Se/Te<31). Pyrite was desulfidized and replaced by troilite during subduction and the coeval prograde metamorphism that affected the recycled components. Fluid-mobile elements (As, Sb, Pb) may have also been released at this stage.

To date no equivalent of Beni Bousera BMS can be found in the diamond-hosted BMS assemblages documented so far although several mineralogical and geochemical features reported in the present study have already been documented in sulphide inclusions of eclogitic affinity. The pyrrhotite major element compositions indicating more oxidized conditions, less diluted bulk sulfide Ni contents or less fractionated S/Se ratios..

ACKNOWLEDGEMENTS : Laurent Lenta is warmly acknowledged for the polished thick sections and Carole La for her help with laser ablation analyses. Thanks are extended to our associate Editor Andreas Audetat, Sonja Aulbach and two anonymous reviewers. Their comments and suggestions greatly improved the manuscript.

FINANCIAL FUNDINGS This work was supported by the « Centre National de la Recherche Scientifique » [UMR 6112]

REFERENCES

Afifi, A.M., Kelly, W.C. & Essene, E.J. (1988). Phase relations among tellurides, sulfides and oxides: I. Thermochemical data and calculated equilibria. *Economic Geology* **83**, 377–394.

Afiri, A., Gueydan, F., Pitra, P., Essaifi, A. & Precigout, J. (2011). Oligo-Miocene exhumation of the Beni-Bousera peridotite through a lithosphere-scale extensional shear zone. *Geodinamica Acta* **24**, 49–60.

Agranier, A., Lee, C.T., Li, Z.X.A. & Leeman, W.P. (2007). Fluid-mobile element budgets in serpentinized oceanic lithospheric mantle: Insights from B, As, Li, Pb, PGEs and Os isotopes in the feather river Ophiolite, California. *Chemical Geology* **245**, 230-241.

Algeo, T.J. & Maynard, J.B. (2004). Trace-element behaviour and redox facies in core shales of Upper Pennsylvanian Kansas-type cyclothems. *Chemical Geology* **206**, 289–318.

Alt, J. (1995). Sulfur isotopic profile through the oceanic crust, sulfur mobility and seawater- crustal sulfur exchange during hydrotyhermal alteration. Geology 23, 585-588.

Andersen, T., Griffin, W.L. & O'Reilly, S.Y. (1987). Primary sulphide melt inclusions in mantle-derived megacrysts and pyroxenites. *Lithos* **20**, 279–294.

Aulbach, S., Creaser, R. A., Pearson, N.J., Simonetti, S.S., Heaman, L. M., Griffin, W., & Stachel, T. (2009). Sulfide and whole-rock Re-Os systematics of eclogite and pyroxenite xenoliths from the Slave Craton, Canada. *Earth and Planetary Science Letter* **283**, 48-58.

Aulbach, S., Stachel, T., Seitz, H.M. & Brey, G.P. (2012). Chalcophile and siderophile elements in sulfide inclusions in eclogitic diamonds and metal cycling in a Paleoproterozoic subduction zone. *Geochimica et Cosmochimica Acta* **93**, 278–299.

Aulbach, S., Woodland, A. B., Vasilyev, P., Galvez, M. E. & Viljoen, K. S. (2017). Effects of low-pressure igneous processes and subduction on $Fe^{3+/}Fe$ and redox state of mantle eclogites from Lace (Kaapvaal craton). *Earth and Planetary Science Letter* **474**, 283-295.

Aulbach, S, Woodland, Alan B., Stern, R. A., Vasilyev, P., Heaman, L. M. & Viljoen, K. S. (2019). Evidence for a dominantly reducing Archaean ambiant mantle from two proxies, and low oxygen fugacity of deeply subducted oceanic crust. *Scientific Report* Dec 27 2019.

Ballhaus, C. & Ulmer, P. (1995). Platinum-group elements in the Merensky Reef: II Experimental solubilities of platinum and palladium in $Fe_{1-x}S$ from 950 to 450°C under controlled fS_2 and fH_2. *Geochimica et Cosmochimica Acta* **59**, 4881-4888.

Ballhaus, C., Tredoux, M. & Späth, A. (2001). Phase relations in the Fe-Ni-Cu-PGE-S system at magmatic temperature and application to massive sulphide ores of the Sudbury Igneous Complex. *Journal of Petrology* **42**, 1991-1926.

Bataleva, Y.V., Palyanov, Y.N., Borzdov, Y.M., Novoselo, D. & Bayuko, O.A. (2019). An effect of reduced S-rich fluids on diamond formation under mantle-slab interaction. *Lithos* **336–337**, 27–39.

Bézos, A., Lorand, J.-P., Hummler, E. & Gros, M (2005) Platinum-group element systematics in Mid-Oceanic Ridge Basaltic glasses from the Pacific, Atlantic and Indian Oceans. *Geochimica et Cosmochimica Acta* **69**, 2613-2627.

Blichert-Toft, J., Albarède, F. & Kornprobst, J. (1999). Lu-Hf isotope systematics of garnet pyroxenites from Beni Bousera, Morocco: implications for basalt origin. *Science* **283**, 1303–1306.

Cabri, L.J. (1965). Phase relations in the Au-Ag-Te systems and their mineralogical significance. *Economic Geology* **60**, 1569–1606.

Cartigny, P. (2005). Stable isotopes and the origin of diamond. *Elements* **1**, 70–84.

Chalouan, A., Michard, A., El Kadiri, K., Negro, F., Frizon de Lamotte, D. & Saddiqi, O. (2008). The Rif Belt. In: Michard, A., Chalouan, A., Saddiqi, O. & Frizon de Lamotte, D. (eds). Continental Evolution: The Geology of Morocco. Springer, pp. 203-302.

Chaussidon, M., Albarède, F. & Sheppard, S.M.F. (1987). Sulphur isotope heterogeneity in the mantle from ion microprobe measurements of sulphide inclusions in diamonds. *Nature* **330**, 242–244.

Clemens, B.M., Haggerty, S. & Harris, J. (2008). Magnetic inclusions in diamonds. *Earth and Planetary Science Letters* **267**, 333-340.

Conquéré, F. & Kornprobst, J. (1972). Quelques précisions sur les caractères minéralogiques et chimiques des pyroxénolites à grenat des Beni Bousera. *Bulletin Société Française de Mineralogie et Cristallographie* **95**, 115-123.

Consuma, G., Aulbach, S., Braga, R., Martin, A.J., Tropper, M.P., Gerdes, A. & Fiorentini, M. (2021). Multi-stage sulfur and carbon mobility in fossil continental subduction zones: New insights from carbonate-bearing orogenic peridotites. *Geochimica et Cosmochimica Acta* **306**, 143-170.

Coveney, R.M. & Glascock, M.D. (1989) A review of the origins of metal-rich Pennsylvanian black shales, central U.S.A., with an inferred role for basinal brines. *Applied Geochemistry* **4**, 347–367.

Coveney, R.M. & Martin, S.P. (1983). Molybdenum and other heavy metals of the Mecca Quarry and Logan

Quarry shales. *Economic Geology* **78**, 132–149.

Craig, J.R. & Kullerud, G. (1969). Phase relations in the Cu-Fe-Ni-S system and their application to magmatic ore deposits. *Economic Geology*, Monography **4**, 344–358.

Crusius, J., Calvert, S.E., Pedersen, T.F. & Sage, D. (1996). Rhenium and molybdenum enrichments in sediments as indicators of oxic, suboxic and sulfidic conditions of deposition. *Earth and Planetary Science Letters* **145,** 65– 78.

Czamanske, G.K. & Moore, J.B. (1977). Composition and phase chemistry of sulfide globules in basalt from the Mid-Atlantic ridge rift valley near 37° N lat. *Geological Society America Bulletin* **88**, 587-599

Day, H.W. (2012). A revised diamond-graphite transition curve. *American Mineralogist* **97**, 52-62.

De Waal, S.A & Calk, L.C. (1975). Sulfides in the garnet -pyroxenite xenoliths from Salt Lake Crater, Oahu, Hawaii. *Journal of Petrology* **16**, 134−153.

Deines, P. & Harris, J.W. (1995). Sulfide inclusion chemistry and carbon isotopes of African diamonds. *Geochimica et Cosmochimica Acta* **59**, 3173–3188.

Eggler, D.H. & Lorand, J.-P. (1993). Mantle sulfide geobarometry. *Geochimica et Cosmochimica Acta* **57**, 2213–2222.

El Atrassi, F., Brunet, F., Bouybaouène, M., Chopin, C. & Chazot, G. (2011). Melting textures and microdiamonds preserved in graphite pseudomorphs from the Beni Bousera peridotite massif, Morocco. *European Journal of Mineralogy* **23**, 157-168.

El Atrassi, F., Brunet, F., Chazot, G., Bouybaouène, M. & Chopin, C. (2013). Metamorphic overprint of garnet pyroxenites/peridotite from the Beni Bousera massif (Northern Morocco): Mineralogical, chemical and textural records. *Lithos* **179**, 231-248.

El Atrassi, F., Chazot, G., Brunet, F., Chopin, C., Bouybaouène, M. (2014). Amphibole genesis in pyroxenites from the Beni Bousera peridotite massif (Rif, Morocco): Evidence for two different metasomatic episodes *Lithos* **208**, 67-80.

Erickson, B. E. & Helz, G. R. (2000). Molybdenum (VI) speciation in sulfidic waters: stability and stability of thiomolybdates. *Geochimica et Cosmochimica Acta* **64**, 1149–1158.

Etschmann, B., Pring A., Putnis, A., Grguric, B A. & Studer, A. (2004). A kinetic study of the exsolution of pentlandite $(Ni,Fe)_9S_8$ from the monosulfide solid solution (Fe,Ni)S. *American Mineralogist* **89,** 39−50.

Evans, K.A., Tomkins, A.G., Cliff J. & Fiorentini, M.L. (2014). Insights into subduction zone sulfur recycling

from isotopic analysis of eclogite-hosted sulfides. *Chemical Geology* **365**, 1–19.

Fleet, M.E. (2006). Phase equilibria at high temperature. In: Vaughan, D. (Ed.), Sulfide Mineralogy and Geochemistry. *Review in Mineralogy and Geochemistry* **61**, 365–419.

Frets, E. C., Tommasi, A., Garrido, C. J., Vauchez, A., Mainprice, D., Targuisti, K. & Amri, I. (2014). The Beni Bousera peridotite (Rif Belt, Morocco): an oblique-slip low-angle shear zone thinning the subcontinental mantle lithosphere. *Journal of Petrology* **55**, 283–313.

Frost, D.J. & Wood, B.J. (1997). Experimental measurements of the fugacity of CO_2 and graphite/diamond stability from 35 to 77 kbar at 925 to 1650 °C. *Geochimica et Cosmochimica Acta* **61**, 1565–1574.

Gadd, M.G., Peter, J.M., Jackson, S.E., Yang, Z. & Petts, D. (2019). Platinum, Pd, Mo, Au and Re deportment in hyper-enriched black shale Ni- Zn-Mo-PGE mineralization, Peel River, Yukon, Canada. *Ore Geology Reviews* **107**, 600–614.

Greaney, A., Rudnick, R.L., Gaschnig, R.M., Whalen, J.B. Luais, B. & Clemens, J.D. (2018). Geochemistry of molybdenum in the continental crust. *Geochimica et Cosmochimica Acta* **238**, 36-54.

Gréau, Y., Alard, O., Griffin, W.L., Huang, J.X., & O'Reilly, S.Y. (2013). Sulfides and chalcophile elements in Roberts Victor eclogites: Unravelling a sulfide-rich metasomatic event. *Chemical Geology* **354**, 73–92.

Gregory, D. D., Large, R. L., Halpin J. A., Bauturina E. L., Lyons T. W., Wu S., Danyushevsky L., Sack P. J., Chappaz, A., Maslennikov, V. V. & Bull, S. W. (2015). Trace element content of sedimentary pyrite in black shales. *Economic Geology* **110,** 1389– 1410.

Gregory, D., Mukherjee, I., Olson, S.L., Large, R.R., Danyushevsky, L.V., Stepanov, A.S., Avila, J.N. Cliff, J., Ireland, T.R., Raiswell, R., Olin, P.H., Maslennikov, V.V. & Lyons, T.W. (2019). The formation mechanisms of sedimentary pyrite nodules determined by trace element and sulfur isotope microanalysis. *Geochimica et Cosmochimica Acta* **259**, 53-68.

Griffin, W.L., Powell, W.J., Pearson N.J. & O'Reilly, S.Y. (2008). GLITTER: Data reduction software for laser ablation ICP-MS. *Mineralogical Association Canada*, Short Course Series **40**, 308–311.

Gysi, A. P., Jagoutz, O., Schmidt, M. W. & Targuisti, K., (2011). Petrogenesis of Pyroxenites and Melt Infiltrations in the Ultramafic Complex of Beni Bousera, Northern Morocco. *Journal of Petrology* **52**, 1679-1735.

Haggerty, S.E. (1986). Diamond genesis in a multiply-constrained model. *Nature* **320**, 34-37.

Hall, A.J. (1986). Pyrite-pyrrhotine redox reactions in nature. *Mineralogical Magazine* **50**, 223-229.

Harris, J.W. (1992). Diamond geology. In: Field, J.E. (Ed.), The Properties of Natural diamonds. John Wiley and Sons, New York, pp. 501–525.

Hedenquist, J.W., Arribas, Jr, A. & González-Urien, E. (2000). Exploration for epithermal gold deposits. *Reviews for Economic Geology* **13,** 245–277.

Helmy, H.M., & Fonseca, R. (2017). The behavior of Pt, Pd, Cu and Ni in the Se-sulfide system between 1050 and 700°C and the role of Se in platinum-group elements fractionation in sulfide melts. *Geochimica et Cosmochimica Acta* **216**, 141–152.

Helmy, H.M., Ballhaus, C., Wohlgemuth-Ueberwasser, C., Fonseca, R.O.C. & Laurenz, V. (2010). Partitioning of Se, As, Sb, Te and Bi between monosulfide solid solution and sulfide melt—application to magmatic sulfide deposits. *Geochimica et Cosmochimica Acta* **74,** 6174–6179.

Helmy H.M. & Botcharnikov, R. (2020). Experimental determination of the phase relations of Pt and Pd antimonides and bismuthinides in the Fe-Ni-Cu sulfide systems between 1100 and 700 °C. *American Mineralogist* **105**, 344–352.

Helz, G.R., Miller, C.V., Charnock, J.M., Mosselmans, J.F.W., Pattrick, R.A.D., Garner, C.D. & Vaughan, D.J. (1996). Mechanisms of molybdenum removal from the sea and its concentration in black shales: EXAFS evidence. *Geochimica et Cosmochimica Acta* **60**, 3631– 3642.

Holwell, D., Stachel, T., Stern, R. A., Pearson, D. G., Nestola, F., Hardman, M. F., Harris, J. W., Jaques, A. L., Shirey, S. B., Cartigny, P., Smit, K.V., Aulbach, S., Brenker, F. E., Jacob, D. E., Thomassot, E., Walter, M. J., & Navon, O. (2020). Deep carbon through time: Earth's diamond record and its implication for carbon cycling. *Geochimica et Cosmochimica Acta* **275**, 99-122.

Holzheid, A. & Grove, T.L. (2002). Sulfur saturation limits in silicate melts and their implications for core formation scenarios for terrestrial planets. *American Mineralogist* **87**, 227–237.

Jenner, F. E., Arculus, R. J., Mavrogenes, J. A. et al. (2012). Chalcophile element systematics in volcanic glasses from the northwestern Lau Basin . *Geochemistry Geophysics System* **13**, Article Number: Q06014.

Jochum, K. P. & Verma, S. P. (1996). Extreme enrichment of Sb, Tl and other trace elements in altered MORB. *Chemical Geology* **130**, 289–299.

Karakaya, I. & Thompson, W. T. (1991). The Ag–Te (Silver– Tellurium) System. *Journal of Phase Equilibria* **12**, 56–63.

Kawakami, T., Ellis, D.J. & Christy, A.G. (2006). Sulfide evolution in high-temperature to ultrahigh-

temperature metamorphic rocks from Lützow–Holm Complex, East Antarctica. *Lithos* **92**, 431−446.

Kelly, D.P. & Vaughan, D.J. (1983). Pyrrhotine-pentlandite ore textures: a mechanistic approach. *Mineralogical Magasine* **47**, 453-463.

Kempinnen, L.I.M., Kohn, S.C., Parkinson, I.J., Bulanova, G.P., Howell, D.H. & Smith, C.B. (2018). Identification of molybdenite in diamond-hosted sulphide inclusions: Implications for Re-Os radiometric dating. *Earth and Planetary Science Letters* **495**, 101–111.

Kitakaze, A., Machida, T. and Komatsu, R. (2016). Phase relations in the Fe–Ni–S system from 875 ºC to 650 ºC. *Canadian Mineralogist* **54**, 1175–1186.

Kornprobst, J. (1969). Le massif ultrabasique des Beni Bouchera (Rif Interne, Maroc): Etude des péridotites de haute température et de haute pression et des pyroxénolites, à grenat ou sans grenat, qui leur sont associées. *Contributions to Mineralogy and Petrology* **23**, 283-322.

Kornprobst, J. (1970). Les péridotites et les pyroxénolites du massif ultrabasique des Beni Bousera; une étude expérimentale entre 1100° et 1550°C sous 15 à 30 kb de pression sèche. *Contributions to Mineralogy and Petrology* **29**, 290-309.

Kornprobst, J., Piboule, M., Roden, M. & Tabit, A. (1990). Corundum bearing garnet clinopyroxenites at Beni Bousera (Morocco): Original plagioclase-rich gabbros recrystallized at depth within the mantle. *Journal of Petrology* **31**, 717-745.

Kumar, N., Reisberg, L. & Zindler, A. (1996). A major and trace element and strontium, neodymium, and osmium isotopic study of a thick pyroxenite layer from the Beni Bousera ultramafic complex of northern Morocco. *Geochimica et Cosmochimica Acta* **60**, 1429-1444.

Labidi J., Cartigny P., Birck J. L., Assayag N., & Bourrand J. J. (2012). Determination of multiple sulfur isotopes in glasses: A reappraisal of the MORB δ^{34}S. *Chemical Geology* **334**, 189–198.

Labidi, J. & Cartigny, P. (2016). Negligible sulfur isotope fractionation during partial melting : Evidence from Garett transform fault basalts, implication for the late-veneer and gthe hadean matte. *Earth and Planetary Science Letters* **451**, 196-207.

Large, R.R., Thomas, H., Craw, D., Henne A., & Henderson, S. (2012). Diagenetic pyrite as a source for metals in orogenic gold deposits, Otago Schist, New Zealand. *New Zealand Journal of Geology and Geophysics* **55**, 137-149.

Large, R.R., Mukherjee, I., Gregory, D.D., Steadman, J.A., Maslennikov, V.V., Meffre, S., (2017). Ocean and

Atmosphere Geochemical Proxies Derived from Trace Elements in Marine Pyrite: Implications for Ore Genesis in Sedimentary Basins. *Economic Geology* **112**, 423-450.

Layton-Matthews, D., Leybourne, M.I., Peter, J.M., Scott, S.D., Cousens, B. & Eglington, B.M. (2013). Multiple sources of selenium in ancient seafloor hydrothermal systems: Compositional and Se, S, and Pb isotopic evidence from volcanic-hosted and volcanic-sediment-hosted massive sulfide deposits of the Finlayson Lake District, Yukon, Canada. *Geochimica et Cosmochimica Acta* **117**, 313–331.

Li C., Barnes S.-J., Makovicky E., Rose-Hansen J. & Makovicky M. (1996). Partitioning of Ni, Cu, Ir, Rh, Pt and Pd between monosulfide solid solution and sulfide liquid: effects of composition and temperature. *Geochimica et Cosmochimica Acta* **60**, 1231–1238.

Li, F. & Franzen, H.F. (1996). Phase transitions in near stoichiometric iron sulfide. *Journal of Alloys and Compounds* **238,** 73-80.

Li, Y., & Audétat, A. (2012). Partitioning of V, Mn, Co, Ni, Cu, Zn, As, Mo, Ag, Sn, Sb, W, Au, Pb, and Bi between sulfide phases and hydrous basanite melt at upper mantle conditions. *Earth and Planetary Science Letters* 355-356, 327–340.

Li, Y., & Audétat, A. (2015). Effects of temperature, silicate melt composition, and oxygen fugacity on the partitioning of V, Mn,Co, Ni,Cu, Zn, As, Mo, Ag, Sn, Sb, W, Au, Pb, and Bi between sulfide phases and silicate melt. *Geochimica et Cosmochimica Acta* **162**, 25-45.

Lissner, M., König, S., Luguet, A., Le Roux, P.-J., Schuth, S., Heuser, A. & le Roex, A.P. (2014). Selenium and tellurium systematics in MORBs from the southern Mid-Atlantic Ridge (47–50°S). *Geochimica et Cosmochimica Acta* **144**, 379–402.

Liu, Y. & Brenan, J. (2015). Partitioning of platinum-group elements (PGE) and chalcogens (Se, Te, As, Sb, Bi) between monosulfide-solid solution (MSS), intermediate solid solution (ISS) and sulfide liquid at controlled fO_2–fS_2 conditions. *Geochimica et Cosmochimica Acta* **159**, 139–161.

Longerich, H. P., Jackson, S. E. & Günther, D. (1996). Laser ablation inductively coupled plasma mass spectrometric transient signal data acquisition and analyte concentration calculation. *Journal of Analytical Atomic Spectrometry* **11**, 899–904.

Lorand, J.-P. (1983). Les minéraux opaques des lherzolites à spinelle et des pyroxénites associées : une étude comparative dans les complexes de lherzolite à spinelle et les enclaves des basaltes alcalins. PhD thesis, 258 pages.

Lorand, J.-P. (1989a). Sulfide petrology of spinel and garnet pyroxenite layers from mantle-derived spinel lherzolite massifs of Ariège (Northeastern Pyrenees, France). *Journal of Petrology* **30**, 989-1015.

Lorand, J.-P. (1989b). The Cu-Fe-Ni sulfide component of the amphibole-rich veins from the Lherz and Freychinède spinel peridotite massifs (Northeastern Pyrenees, France) ; a comparison with mantle-derived megacrysts from alkali basalts. *Lithos* **23**, 281-299.

Lorand, J.-P. & Alard, O. (2010). Determination of selenium and tellurium concentrations in Pyrenean peridotites (Ariège, France); New insight into S/Se/Te systematics of the upper mantle. *Chemical Geology* **278**, 120-130.

Lorand, J.-P. & Grégoire M. (2006). Petrogenesis of base metal sulfides of some peridotites of the Kaapvaal craton (south Africa). *Contributions to Mineralogy Petrology* **151**, 521-538.

Lorand, J.-P. & Luguet, A., (2016). Chalcophile/siderophile elements in mantle rocks : trace elements controlled by trace minerals. *Review in Mineralogy and Geochemistry* **81**, 441-488.

Lorand, J.-P., Hewins, R. H. Humayun, M., Zanda, B., Remusat L., La, C. & Pont, S. (2018). Chalcophile-siderophile element systematics of hydrothermal pyrite from martian regolith breccia NWA 7533. *Geochimica Cosmochimica Acta* **241**, 134-149.

Luguet, A., Lorand, J.-P., Alard, O. & Cottin, J.Y. (2004). A multi-technique study of platinum-group elements systematic in some Ligurian ophiolitic peridotites, Italy. *Chemical Geology* **208**, 175-194.

Luguet, A., Pearson, D.G., Nowell, G.M., Dreher, S.D., Coggon, J.A., Spetsius, Z.D. & Parman, S.W. (2008). Enriched Pt-Re-Os Isotope Systematics in Plume Lavas Explained by Metasomatic Sulfides. *Science* **319**, 453-456.

Mansur, E.T. & Barnes, S.-J. (2020). Concentrations of Te, As, Bi, Sb and Se in the Marginal Zone of the Bushveld Complex: Evidence for crustal contamination and the nature of the magma that formed the Merensky Reef. *Lithos* **358–359**, 105407.

Maslennikov, V.V., Maslennikova, S.P., Large, R.R., & Danyushevsky, L.V. (2009). Study of trace element zonation in vent chimneys from the Silurian Yaman-Kasy VMS (the Southern Urals, Russia) using laser ablation inductively coupled plasma mass spectrometry (LA-ICP MS). *Economic Geology* **104**, 1111–1141.

Mathez, E.A. (1976). Sulfur solubility and magmatic sulfides in submarine basalt glass. *Journal of Geophysical Research* **81(23)**, 4269-4276.

Mauffret, A., Ammar, A., Gorini, C. & Jabour, H. (2007). The Alboran Sea (Western Mediterranean) revisited

with a view from the Moroccan Margin. *Terra Nova* **19**, 195–203.

Mavrogenes, J. & O'Neill, H.S.C. (1999). The relative effects of pressure, temperature and oxygen fugacity on the solubility of sulfide in mafic magmas. *Geochimica Cosmochimica Acta* **63**, 1173−1180.

Mc Queen, K.G. (1979). Experimental heating and diffusion effects in Fe-Ni sulfide ores from Redross, Western Australia. *Economic Geology* **74**, 140-148.

McDonald, I., Hughes, H.S.R., Butler, S., Harris, J.W. & Muir, D. (2017). Homogenisation of sulphide inclusions within diamonds: A new approach to diamond inclusion geochemistry. *Geochimica et Cosmochimica Acta* **216,** 335-357.

Mengason, M. J., Candela, P. A. & Piccoli, P. M. (2011). Molybdenum, tungsten and manganese partitioning in the system pyrrhotite–Fe–S–O melt–rhyolite melt: impact of sulfide segregation on arc magma evolution. *Geochimica et Cosmochimica Acta* **75**, 7018–7030.

Meyer, H.O. A. (1987). Inclusions in diamond. In: Nixon, P.H.E. (Ed.), Mantle Xenoliths.

Montanini, A., Tribuzio, R. & Bersani, D. (2010). Insights into the origin of mantle graphite and sulfides in garnet pyroxenites from the External Ligurides peridotites (Northern Apenine, Italy). *Geological Society of London, Special publication*, London **337**, 87-105.

Nakazawa, H., & Morimoto, N. (1971). Phase relations and superstructures of pyrrhotite, $Fe_{1-x}S$. *Materials Research Bulletin* **6**, 345-358.

Noll, P. D., Newsom, H. E., Leeman, W. P. & Ryan, J. G. (1996). The role of hydrothermal fluids in the production of subduction zone magmas: Evidence from siderophile and chalcophile trace elements and boron. *Geochimica et Cosmochimica Acta* **60**, 587–611.

Palme, H. & O'Neill, H. S. C. (2014). Cosmochemical estimates of mantle composition. In « Treatise on Geochemistry, » vol. 2 (eds. H. D. Holland, K. K. Turekian and R. W. Carlson). Elsevier Pergamon, Amsterdam, pp. 1–38.

Pals, D.W. & Spry, P.G. (2003). Telluride mineralogy of the low-sulfidation epithermal Emperor gold deposit, Vatukoula, Fiji. *Mineralogy and Petrology* **79**, 285–307.

Palyanov, Y. N., Borzdov, Y. M., Bataleva, Y.V., Sokol, A.G., Palyanova, G.A. & Kupriyanov, I.N. (2007). Reducing role of sulfides and diamond formation in the Earth's mantle. *Earth and Planetary Science Letters* **260**, 242–256.

Parnell, J., Perez, M., Armstrong, J., Bullock, L. Feldmann, J. & Boyce, A.J. (2018). Geochemistry and

metallogeny of Neoproterozoic pyrite in oxic and anoxic sediments *Geochemical Perspective Letter* **7**, 12-16.

Pasava, J., Ackerman, L., Haldová, P., Pour, O., Ďurisová, J., Zaccarini, F., Aiglsperger, T. & Vymazalová, A. (2017). Concentrations of platinum-group elements (PGE), Re and Au in arsenian pyrite and millerite from Mo–Ni–PGE-Au black shales (Zunyi region, Guizhou Province, China): results from LA-ICPMS study. *European Journal of Mineralogy* **29**, 623-633.

Pasteris, J.D. (1985). Relationships between temperature and oxygen fugacity among Fe-Ti oxides in two regions of the Duluth complex. *Canadian Mineralogist* **23**, 111-127.

Patten, C., Barnes, S.J. & Mathez, E. (2012). Textural variations in MORB sulfide droplets due to difference in crystallization history. *Canadian Mineralogist* **50**, 675-692.

Patten, C., Barnes, S., Mathez E. A. & Jenner, F. E. (2013). Partition coefficients of chalcophile elements between sulfide and silicate melts and the early crystallization history of sulfide liquid: LA-ICP-MS analysis of MORB sulfide droplets. *Chemical Geology* **358**, 170–188.

Patterson, J.H., Ramsden, A.R., Dale, L.S. & Fardy, J.J. (1986). Geochemistry and mineralogical residences of trace elements in oil shales from Julia Creek, Queensland, Australia. *Chemical Geology* **55**, 1–16.

Pearson, D. G. & Nowell, G. M. (2004). Re-Os and Lu-Hf Isotope constraints on the origin and age of pyroxenites from the Beni Bousera Peridotite Massif: Implications for mixed peridotite-pyroxenite mantle sources. *Journal of Petrology* **45**, 439–455.

Pearson, D. G., Davies, G. R. & Nixon, P. H., (1993). Geochemical constraints on the petrogenesis of diamond facies pyroxenites from the Beni Bousera peridotite massif, North Morocco. *Journal of Petrology* **34**, 125–172.

Pearson, D. G., Davies, G. R. & Nixon, P. H. (1995). Orogenic ultramafic rocks of UHP (diamond facies) origin. In: Coleman, R. G. & Wang, X. (eds.) Ultrahigh Pressure Metamorphism. Cambridge: Cambridge University Press, 456–510.

Pearson, D.G., Davies, G.R., Nixon, P.H. & Mattey, D.P. (1991). A carbon isotope study of diamond facies pyroxenites and associated rocks from the Beni Bousera peridotite, North Morocco. *Journal of Petrology* Special Lherzolites Issue: 175–189.

Pearson, D.G., Davies, G.R., Nixon, P.H. & Milledge, H.J., (1989). Graphitized diamonds from a peridotite massif in Morocco and implications for anomalous diamond occurrences. *Nature* **335**, 60-66.

Pedersen, A. K. (1979). Basaltic glass with high-temperature equilibrated immiscible sulphide bodies with native iron from Disko, central west Greenland. *Contributions to Mineralogy and Petrology* **69,** 397–407.

Peregoedova, A., Barnes, Sarah-Jane & Baker, D.R. (2004) The formation of Pt-Ir alloys and Cu-Pd-rich sulfide melts by partial desulfuration of Fe-Ni-Cu sulfides: results of experiments and implications for natural systems. *Chemical Geology* **208**, 247-264.

Peterson, R. & Francis, D. (1977) The origin of sulfide inclusions in pyroxene megacrysts. *American Mineralogist* **50**, 1049–1051.

Pokrovski, G.S., Zakirov, I.V., Roux, J., Testemale, D, Hazemann, J.L., Bychkov, A.Y. & Golikova, G.V. (2002) Experimental study of arsenic speciation in vapour phase to 500 C: implication for As transport and fractionation in low-density crustal fluids and volcanic gases. *Geochimica Cosmochimica Acta* **66**, 3453–3480.

Power, L.F. & Fine, H.A. (1976) The iron-sulfur system. Parts 1.- The structures and physical properties of the compounds of the low-temperature phase fields. *Minerals and Science engineering* **8**, 106-128.

Puchelt, H., Prichard, H.M., Berner, Z. & Maynard, J. (1996). Sulfide mineralogy, sulfur content, and sulfur isotope composition of mafic and ultramafic rocks from Leg 147. In: Mevel, C., Gillis, K.M., Allan, J.F., Meyer, P.S. (Eds.). *Proceedings of the Ocean Drilling Program,* Scientific Results, **147**, 5, 91-101.

Queffurus, M. & Barnes, Sarah.-J. (2015). A review of sulfur-to-selenium ratios in magmatic nickel– copper and platinum-group element deposits. *Ore Geology Review* **69**, 301-324.

Rimmer, S.M. (2004). Geochemical paleoredox indicators in Devonian-Mississippian black shales, Central Appalachian Basin, USA. *Chemical Geology* **206**, 373–391.

Rudnick, R.L. & Gao, S. (2014). Composition of the Continental Crust. In Treatise on Geochemistry, Volume **4** (pp.1-51). Second edition Elsevier Editors: H. D. Holland, K. K. Turekian.

Ryzhenkho, B., & Kennedy, G.C. (1973). Effect of pressure on eutectic in system Fe-FeS. *American Journal of Science* **273**, 803–810.

Samalens, N., Barnes, Sarah-J. & Sawyer, E.W. (2017). The role of black shales as a source of sulfur and semimetals in magmatic nickel-copper deposits: Example from the Partridge River Intrusion, Duluth Complex, Minnesota, USA. *Ore Geology Reviews* **81**, 173-187.

Schirmer , T., Koschinsky, A. & Bau, M. (2014). The ratio of tellurium and selenium in geological material as a possible paleo-redox proxy. *Chemical Geology* **376**, 44–51.

Schulze, R.B. (2004). Geochemical relationships of Late Paleozoic carbon-rich shales of the Midcontinent, USA: a compendium of results advocating changeable geochemical conditions. *Chemical Geology* **206**, 347– 372.

Sen, I.S., Bizimis M. & Sen G. (2010). Geochemistry of sulfides in Hawaiian garnet pyroxenite xenoliths: Implications for highly siderophile elements in the oceanic mantle. *Chemical Geology* **273**, 180–192.

Shaw, C.S.J. (1997). Origin of sulfide blebs in variably metasomatised mantle xenoliths, quaternary West Eifel volcanic Field, Germany. *Canadian Mineralogist* **35**, 1453– 1463.

Shawar, L., Halevy T., Ward, S.A., Feinstein, S. Boyko, V., Kamyshn, A. and Amrani, A. (2018). Dynamics of pyrite formation and organic matter sulfurization in organic-rich carbonate sediments. *Geochimica et Cosmochimica Acta* **241**, 219–239.

Shirey, S.B., Cartigny, P., Frost, D.G., Keshav, S., Nestola, F., Nimis, P., Pearson, D.G., Sobolev, N.V. & Walter, M.J. (2013). Diamonds and the geology of mantle carbon. *Review in Mineralogy and Geochemistry* **75**, 355–421.

Simon, G., Kesler, S.E. & Essene, E.J. (1997). Phase relations among selenides, sulfides, tellurides, and oxides: II. Applications to selenide-bearing ore deposits. *Economic Geology* **92**, 468–484.

Slodkevich, V.V. (1980). Polycrystalline aggregates of octahedral graphite. *Doklady* **253**, 194-196. [Translated from Doklady Akademii Nauk SSSR, 253, No. 3, 697700].

Stachel, T. & Harris, J. W. (2008). The origin of cratonic diamonds– constraints from mineral inclusions. *Ore Geology Review* **34**, 5–32.

Stagno, V. & Fei, Y. (2020). The redox boundaries of Earth's Interior. *Elements* **16**, 167-172.

Thomassot, E., Cartigny, P., Harris, J.W., Lorand, J.-P, Rollion-Bard, C. & Chaussidon, M. (2009). Metasomatic diamond growth and its implications on diamond dating: A multi-isotope study (13C, 15N, 33S, 34S) of sulphide-bearing diamonds from Jwaneng (Bostwana). *Earth and Planetary Science Letters* **282**, 79-90.

Toulmin, P., & Barton, P. B. (1964) A thermodynamic study of pyrite and pyrrhotite. *Geochimica et Cosmochimica Acta* **68**, 641–671.

Ulmer, P. & Luth, R.W. (1991). The graphite-COH fluid equilibrium in P, T and fO_2 space. *Contributions to Mineralogy and Petrology* **106**, 265-272.

Van Acken, D., Becker, H., Walker, R.J., Mc Donough, W.F., Wombacher, F., Ash, R.D. & Piccoli, PM. (2010)

Formation of pyroxenite layers in the Totalp ultramafic massif (Swiss Alps)—Insights from highly siderophile elements and Os isotopes. *Geochimica et Cosmochimica Acta* **74**, 661-683.

Van Hinsbergen, D. J. J., Vissers, R. L. M. & Spakman, W. (2014). Origin and consequences of western Mediterranean subduction, rollback, and slab segmentation. *Tectonics* **33**, 2013TC003349.

Varas-Reus, M.I., Garrido C., Marchesi, C., Bosch, D. & Hidas, K. (2018). Genesis of ultra-high pressure garnet pyroxenites in orogenic peridotites and its bearing on the compositional heterogeneity of the Earth's mantl. *Geochimica et Cosmochimica Acta* **232**, 303–328.

Walter, J.B., Cruz-Uribe, A.M. & Marschall**,** H.R. (2020). Sulfur loss from subducted altered oceanic crust and implications for mantle oxidation. *Geochemical Perspective Letter* **13**, 36-41.

Wang, H. & Salveson, I. (2005). A review on the mineral chemistry of the nonstoichiometric iron sulphide, $Fe_{1-x}S$ ($0 \leq x \leq 0.125$): polymorphs, phase relations and transitions, electronic and magnetic structures. *Phase Transitions* **78**, 547-567.

Wang, Z. & Becker, H. (2013). Ratios of S, Se and Te in the silicate Earth require a volatile-rich late veneer. *Nature* **499**, 328–331.

Wang, Z., Jina, Z.H., Mungall, J.E. & Xiao, X. (2020). Transport of coexisting Ni-Cu sulfide liquid and silicate melt in partially molten peridotite. *Earth and Planetary Science Letters* **536**, 116162.

Wilson S.A., Ridley, W.I. & Koenig, A.E. (2002). Development of sulfide calibration standards for the laser ablation inductively-coupled plasma mass spectrometry technique. *Journal of Analytical Atomic Spectroscopy* **17**, 406–409.

Wohlgemuth-Ueberwasser, C., Fonseca, R. O. C. & Laurenz, V. (2010). Partitioning of Se, As, Sb, Te and Bi between monosulfide solid solution and sulfide melt – application to magmatic sulfide deposits. *Geochimica et Cosmochimica Acta* 74, 6174–6179.

Yang, K. & Scott, S.D. (2002). Magmatic degassing of volatiles and ore metals into a hydrothermal system on the modern sea floor of the eastern Manus back-arc basin, western Pacific. *Economic Geology* **97**, 1079–1100.

Yefimova, E.S., Sobolev, L.N. & Pospelova, L .N. (1983). Inclusions of sulfides in diamond and their paragenesis. *Zap. Vses. Mineral.* **CXII,** 300–309.

Zdrokov, E., Novoselov, Y., Bataleva, Y., Borzdov Y. & Palyanov., Y. (2019). Experimental Modeling of Silicate and Carbonate Sulfidation under Lithospheric Mantle P,T-Parameters. *Minerals* **9**, 425.

Table 1. Base metal sulphide (BMS) modal abundance and BMS phases in Beni Bousera garnet pyroxenites.

sample number	petrographic type	S (µg/g)	Cu (µg/g)	BMS modal abundance (wt.%)	BMS modal abundance	BMS assemblage	Cp weight fraction	Fe-Ti oxide modal abundance
				(calculated)	(visual estimation)		(100% BMS)	(visual estimation)
3408	garnet clinopyroxenite	1210	23.5	0.33	x	Po (PnCp)	2.0	xx
3208	garnet clinopyroxenite	1685	32.1	0.45	xx	Po (PnCp)	2.0	x
11PY	garnet clinopyroxenite	1505	41.9	0.43	x	Po (PnCp)	3.0	xx
3008	garnet websterite	2240	34.6	0.6	xx	Po (Cp,Pn)	1.7	xxx
2008	garnet clinopyroxenite	1650	38.8	0.45	x	Po (Pn)	2.6	x
3108	graphite garnet clinopyroxenite	2900	26.0	0.8	xx	Po (Pn,Cp)	1.0	xxx
3308	graphite garnet clinopyroxenite	5586	31.2	1.5	xxx	Po (Pn,Cp)	0.6	x
2308	graphite garnet clinopyroxenite	5550	30.3	1.5	xxx	Po ((Cp,Pn))	0.6	xx

x : trace mineral (<10 grains per standard polished thin section); xx: minor mineral (10-50 grains per standard polished thin section); xxx : major mineral (>100 grains per standard polished thin section); Sulfide modal abundances were calculated from bulk-rock S contents assuming that S is mainly hosted in pyrrhotite of troilite composition.

Po = pyrrhotite; Pn = pentlandite; Cp = chalcopyrite; Cp modal abundance in 100 wt.% BMS were recomputed from bulk-rock Cu/S ratio.

Table 2. Major element contents of Base Metal Sulphides (Electron Microprobe Analyses).

	Pyrrhotite-troilite intergrowth									
3208 (GP)	Tr	Tr	Po	Po	Tr	Tr	**Pn**	Pn	Pn	Pn
S (wt.%)	36.43	36.49	38.00	38.25	36.51	36.41	33.83	33.38	33.20	33.41
Fe (wt.%)	62.90	63.55	60.92	60.76	62.57	63.51	35.87	35.22	35.32	35.63
Co (wt.%)	<0.05	<0.05	<0.05	<0.05	<0.05	<0.05	2.06	1.97	2.06	2.06
Ni (wt.%)	<0.05	<0.05	0.24	0.29	<0.05	<0.05	28.68	28.93	29.34	27.67
Cu (wt.%)	0.07	0.10	0.0	0.03	0.035	<0.05	<0.05	<0.05	<0.05	<0.05
Total	99.41	100.15	99.17	99.33	99.12	99.95	100.43	99.55	99.94	98.8
S (at.%)	50.21	50.00	52.1	52.37	50.40	49.96				
Fe (at.%)	49.78	49.99	47.9	27.63	49.60	50.00				
2308 (GGP)	Tr	Tr	Tr	Tr	Tr	Tr	Tr	**Tr**	Tr	Tr
S (wt.%)	36.8	36.83	36.8	36.83	36.61	36.7	36.50	36.40	36.52	36.32
Fe (wt.%)	62.98	63.17	62.98	63.17	63.67	63.53	63.61	63.10	64.25	63.62
Co (wt.%)	<0.05	<0.05	<0.05	<0.05	<0.05	<0.05	<0.05	<0.05	<0.05	<0.05
Ni (wt.%)	0.06	0.06	0.06	0.06	<0.05	<0.05	<0.05	<0.05	<0.05	0.08
Cu (wt.%)	0.12	0.09	0.12	0.09	0.07	0.08	0.05	0.06	<0.05	0.03
Total	99.97	100.16	99.97	100.16	100.36	100.34	100.17	99.58	100.8	100.07
S (at.%)	50.43	50.43	50.43	50.36	50.03	50.16	49.98	50.15	49.98	50.11
Fe (at.%)	49.57	49.57	49.57	49.63	49.96	49.85	50.01	49.88	50.66	50.03
3308 (GGP)	Tr	Tr	Tr	Cp	Cp	Cp	Cp	Cp	Cp	Cp
S (wt.%)	36.45	36.64	36.18	34.21	34.47	34.59	34.19	34.60	34.33	34.24
Fe (wt.%)	63.51	63.32	62.78	30.55	30.70	30.72	29.99	30.44	30.43	30.91
Co (wt.%)	<0.05	<0.05	<0.05	<0.05	<0.05	<0.05	<0.05	<0.05	<0.05	0.02

Ni (wt.%)	<0.05	0.07	0.1	0.16	0.13	n.d.	0.10	<0.05	<0.05	0.25
Cu (wt.%)	0.05	0.07	0.08	34.06	33.58	33.86	33.77	33.28	33.41	33.52
Total	100.01	100.12	99.14	99.00	98.89	99.32	98.07	98.34	98.19	98.97
S (at.%)	50.00	49.97	50.31							
Fe (at.%)	50.00	50.03	49.69							
	graphite garnet clinopyroxenites (Lorand, 1983)					mean troïlite composition (this study)			(Lorand 1983)	
	Tr	Tr	Tr			n = 16			n = 20	
S (wt.%)	36.72	36.70	36.34			36.51 (0.33)			36.60 (0.24)	
Fe (wt.%)	63.05	63.65	63.59			63.22 (0.33)			63.40 (0.28)	
Co (wt.%)	<0.05	<0.05	<0.05			<0.05			<0.05	
Ni (wt.%)	<0.05	<0.05	0.16			<0.05			<0.05	
Cu (wt.%)	<0.05	<0.05	<0.05			<0.05			<0.05	
Total	99.82	100.35	100.09			99.73			100.00	
S (at.%)	50.20	50.11	49.9			50.15 (0.28)			50.13 (0.27)	
Fe (at.%)	49.80	49.89	50.1			49.85 (0.29)			49.87 (0.28)	

GP : garnet clinopyroxenite ; GGP : graphite garnet clinopyroxenite

Table 3. Scanning Electron Microscope identification of metallic trace phases in Beni Bousera garnet pyroxenites.

Sample.	3208	3008	3308	2308
Petrographic type	GP	GW	GGP GGP	
PbTe		+	+	+*
AgTe	+		+	
MoS_2		+	+	+
$PtAs_2$		+**		
PbS		+***	+	+

GP : garnet clinopyroxenite; GW : garnet websterite ; GGP : graphite garnet clinopyroxenite; * = enclosed in garnet; ** = associated with molybdenite; *** = Ag and Sb were detected along with Pb and S.

Table 4. Recomputed bulk composition of Base Metal Sulphides.

	GP		**GW**		**GGP**		**GGP**		**GGP**	
	3208	1 sigma	**3008**	1 sigma	**3108**	1 sigma	**2308**	1 sigma	**3308**	1 sigma
Fe (wt.%)	60.86	2.94	64.02	2.05	61.22	3.7	62.85	1.5	62.03	3.0
Ni (wt.%)	0.21	0.22	0.21	0.17	0.43	0.08	0.16	0.09	0.12	0.14
Cu (wt.%)	0.7 R 0.03 M	0.04	0.58 R 0.21 M	0.33	0.34 R 0.05 M	0.006	0.20 R 0.06 M	0.09	0.20 R 0.003 M	0.003
Co (µg/g)	160	154	160	221	646	1269	156	54	185	185
Zn (µg/g)	143	0.05	57	63	45	45	20.6	20	36	6.5
Ga (µg/g)	0.55	0.1	0.55	5.3	0.9	0.65	1.01	0.82	0.41	0.12
As (µg/g)	2.16	0.8	4	7.4	2.3	0.78	1.5	0.24	1.65	0.3
Se (µg/g)	45.9	2.1	25.5	5.5	21	8	22.2	4.96	28	7
Mo (µg/g)	8.4	0.16	3.1	2.61	11	16	11.6	12	10.5	8.34
Ag (µg/g)	2.41	5.5	0.25	0.05	0.5	0.72	0.02	0.008	0.06	0.04
Pd (µg/g)	0.12	0.66	0.65	0.45	0.23	0.3	0.05	0.02	0.13	0.4
Cd (µg/g)	0.48	7	0.39	0.11	2.05	4.95	0.2	0.07	0.24	0.16
In (µg/g)	0.04	1.96	0.08	0.04	0.11	0.23	0.006	0.001	0.03	0.001
Sn (µg/g)	0.16	0.09	0.21	0.15	0.18	0.05	0.25	0.22	0.15	0.02
Sb (µg/g)	0.05	0.01	0.03	0.02	0.033	0.02	0.1	0.03	0.03	0.01
Te (µg/g)	2.85	7.5	1.45	0.73	1.2	0.7	0.67	0.34	1.04	0.69
Os (µg/g)	0.05	0.02	0.47	0.17	0.07	0.04	1.27	2.04	0.06	0.004
Ir (µg/g)	0.01	0.03	0.13	0.09	0.03	0.01	0.06	0.02	0.09	0.004
Pt (µg/g)	0.04	0.02	0.26	0.13	0.02	0.007	0.2	0.06	0.015	0.005
Au (µg/g)	0.2	0.5	0.14	0.06	0.11	0.16	0.11	0.03	0.03	0.01
Tl (µg/g)	0.4	0.5	0.19	0.38	0.13	0.19	0.04	0.009	0.02	0.01
Pb (µg/g)	0.21	0.9	5.2	3.53	0.17	0.3	3.24	3.48	0.03	0.02
Bi (µg/g)	0.21	0.13	0.06	0.02	0.3	0.3	2.14	1.66	0.02	0.02

GP : garnet clinopyroxenite; GW : garnet websterite; GGP : graphite garnet clinopyroxenite. R : Recomputed from bulk-rock Cu contents assuming
36.5 wt.% S in 100 wt.% BMS; M : weighted mean composition from LA-ICPMS analyses; note the strong discrepancy between both results
which likely results from the inability of LA-ICPMS analyses of intercepting chalcopyrite blebs that are inhomogeneously distributed.

Table 5 : Hypothetical bulk composition (X) produced by mixing 5-20% MORB-hosted Base Metal Sulphides (BMS) with 95-80% shale-hosted sedimentary pyrite (μg/g).

	MORB BMS	Sedimentary pyrite (n=1407)	X
Ni	66,400 (28,000)	407-427	6,700-17,400
Os	0.38 (0.51)	<0.05	<0.05-0.11
Ir	0.18 (0 .27)	<0.05	<0.05-0.076
Pt	2.37 (3.44)	0.05-0.1	0.14-0.55
Pd	8.32 (1.67)	0.05-0.1	0.51-1.74
Au	1.16 (0.88)	0.016-0.03	0.085-0.41
Cu	76,000 (34,000)	184-199.9	5,200-14,000
Te	14.6 (3.3)	0.48-0.52	1.5-2.5
Ag	29 (8.8)	2-2.2	3.8-5.8
Se	113(14)	19.5-21.0	23.5-46.2
Cd	13.1 (3.5)		
Bi	3.0 (0.4)	2.3	1.9-2.2
Pb	18.6 (3.5)	140.7-181.8	152.3-170
Sb	0.05	19.5-23.2	15.5-22.0
As	2.8 (2.0)	429-489	343-465
In			
Tl		2.6-3.5	2.5-3.4
Sn	7.42 (1.45)		
Mo	0.45 (0.15)	15.0-20	12.1-19.1
Zn	275 (43.4)	24.9-27.7	35.2-85.7
S	347,100 (5,000)	534,000	
S/Se	3,071.7 (400)	26,700	21,500-25,500
Se/Te	7.4 (3.6)	37.5-43.7	32.1-41.7

MORB BMS composition after Patten et al. (2013) ; Sedimentary pyrite after Gregory et al. (2019). the numbers in parentheses for MORB-hosted BMS are one sigma. The data for sedimentary pyrite show ranges. The values for X propagate minimum and maximum values from MORB-hosted BMS and sedimentary pyrite.

FIGURE CAPTIONS

Figure 1. Geographical location and schematic map of the Beni Bousera peridotite massif in the Betico-Rifean orogenic belt (Northern Morocco) (after Kornprobst et al. (1990), Pearson and Nowell (2004) and El Atrassi et al. (2013). The star indicates the location of the studied samples. The numbers in red correspond to the pyrrhotite compositions reported by Lorand (1983) in garnet pyroxenites from the Ariegite subfacies.

Figure 2. a : Low-magnification image of sample 2308 showing the porphyroclastic texture of graphite garnet clinopyroxenites ; Cpx1 and Gt1 are primary clinopyroxene and garnet. b ; reflected light photomicrograph showing the different generations of exsolutions (garnet-Gt2 and orthopyroxene-Opx2) within a Cpx1 porphyroclast (delineated by a white line). Polyedral grains of yellow-white base metal sulphides (BMS) occur between Cpx1 and Gt1 as well as inside fractured area within Cpx1. c : anhedral BMS grains (yellow white) within Gt1 ; note that all these « included » grains are actually connected with fracture planes and actually represent pseudo-inclusions of former intergranular BMS. d : elongated intergranular BMS (yellow white) truncated and dispersed within the recrystallized matrix of porphyroclastic microtexture. e : Ti-amphibole and ilmenite (ilm) overgrowth on intergranular BMS (yellow white). f : BMS-graphite association ; note the tiny sulphide blebs intercalated betwen graphite lamelae (red arrow). Gr : graphite ; Gt2 ; recrystallized garnet exsolution.

Figure 3. Putative decompression path recorded by Beni Bousera graphite garnet clinopyroxenites (see text for explanations of Stages I to VI, after El Atrassi et al. (2011, 2013)). 1 : lherzolitic solidus. 2,3 liquidus and solidus of garnet pyroxenite compositions (Sen et al., 2010 ; Kornprobst et al., 1970). 4 : troilite liquidus curve (Rhyzenkho and Kennedy, 1973 ; 4P = Palyanov et al., 2007). Graphite-diamond transition curve after Day (2012). Gt : garnet lherzolite domain; Sp : spinel lherzolite domain; Pla : plagioclase lherzolite domain; Ar : Ariegite subdomain; Se : Seiland subdomain.

Figure 4. Backscattered electron (BSE) images of Fe-Ni-Cu sulphides from Beni Bousera pyroxenites. a : Partly weathered intergranular pyrrhotite bleb showing coarse grained pentlandite (Pn) mantled by micron-thick darker rim identified as violarite (EDS spectra). Note supergene weathering features (i.e. cleavage planes in the pyrrhotite (Cl Po) and dark grey rim of pyrrhotite composition that preferentially develops toward the grain margin (sample 3208). b : semi-quadrangular sulfide blebs composed of a sigmoïdal intergrowth between troïlite (Tr) and pyrrhotite (Po) cross cut by a continuous pentlandite exsolution (Pn) with parallel edges (sample 3208). c :

coarse-grained pentlandite (Pn) inside troilite grain-Tr (sample 3308). d : intergranular troilite blebs displaying two generations of pentlandite exsolutions (Pn I and II); see text for further explanation (sample 3308).

Figure 5. Compositional range of pyrrhotite compositions analysed in Beni Bousera garnet pyroxenites. Simplified low-T phase diagram of the central part of the Fe-S system after Power and Fine 1976). The different pyrrhotite superstructures are from Nakazawa and Morimoto (1971). Tr : troilite; mss : monosulphide solid solution..

Figure 6. BSE images of metallic trace phases associated with BMS in Beni Bousera garnet pyroxenites. PbTe : lead telluride; AgTe : silver telluride; Mo : molybdenite (MoS_2); Spe : sperrylite ($PtAs_2$); Au : native gold; Tr : troïlite.

Figure 7. Fe vs. Ni and Cu vs. Ni plots (LA-ICPMS analyses). Tr : troilite ; Po : pyrrhotite ; Pn : pentlandite ; Cp : chalcopyrite.

Figure 8. Ag vs. Te, Te vs. Cu and In vs. Cu plots (LA-ICPMS analyses). Note the positive correlation between In and Cu in sample 3208.

Figure 9. Te vs. Se plot (LA-ICPMS analyses). Note the Te and Se enrichment of sample 3208 compared to the other pyroxenites. The circles in the inset outline the range for each individual graphite garnet clinopyroxenite sample.

Figure 10. Se vs. As and Bi vs. Sb plots (LA-ICPMS analyses).

Figure 11. Mo vs. Tl and Pb vs. Mo plot (LA-ICPMS analyses). Note the Mo enrichment of pyrrhotites.

Figure 12. Projection in the Fe-Ni-S (A) and Fe-Cu-S systems (B) of bulk sulphide compositions of Beni Bousera garnet pyroxenites (at. %). Mss : monosulphide solid solution ; FeS_2 : pyrite; NiS_2 : vaesite. Phase relations and compositional ranges of mss from Craig & Kullerud (1969). The gray field in Fig. 12A delineates the compositional range of mss at 1100 °C.

Figure 13. Schematic fS_2 (fugacity) vs. fO_2 diagram for the main phases expected to coexist in the Fe-

S-O system during the decompression path of Beni Bousera graphite-garnet pyroxenites within the mantle (after Hall, 1986 and Lorand & Grégoire, 2006). Location of the C-CO-CO_2 equilibrium (vertical grey bars) at 1 bar after Ulmer & Luth (1991) and Stagno & Fei (2020) for 5 GPa. Diamond at 5 GPa allows maximum fO_2 corresponding to iron-wustite+2.8 log unit (Stagno and Fei, 2020) and coexisting pyrrhotite composition within the compositional range of troilite (49.3 at.% Fe; black arrow). Pyrrhotite compositions (at.% Fe) after Toulmin & Barton (1974) at 900°C. Mt : magnetite; W : wustite; Po : pyrrhotite; Tr : troilite. The axes are left unlabelled as the values of fS_2 and fO_2 vary greatly with temperature but the geometry of the diagram changes little.

Figure 14. Primitive-mantle normalized chalcophile-siderophile element concentration calculated for pyroxenitic BMS from Beni Bousera (weighted mean composition). The element order was selected as broadly reflecting increasing compatibility in the continental crust (Rudnick and Gao, 2014). Also shown for comparison : shale-hosted sedimentary pyrite compositions, MORB-hosted BMS compositions and the composition of Banded Pyrrhotite Unit (BPU) representing black shale country rocks assimilated by the Duluth igneous complex, Minnesota (Samalens et al., 2017). Note the strongly depleted volatile chalcophile element compositions of Beni Bousera BMS compared to sedimentary pyrite and BPU. Model BMS : putative base metal sulphide compositions calculated by mixing MORB-hosted BMS with shales-hosted sedimentary pyrite (pyrite/BMS weight ratio of 5; see text for more details). Primitive Mantle normalizing values after Palme & O'Neill (2014).

Figure 15. Comparison of mean chalcophile siderophile element compositions of Beni Bousera pyroxenitic BMS with BMS enclosed in eclogitic diamonds. The Aulbach et al (2012) data represent the range for minimum and maximum values. Primitive Mantle normalizing values after Palme & O'Neill (2014).

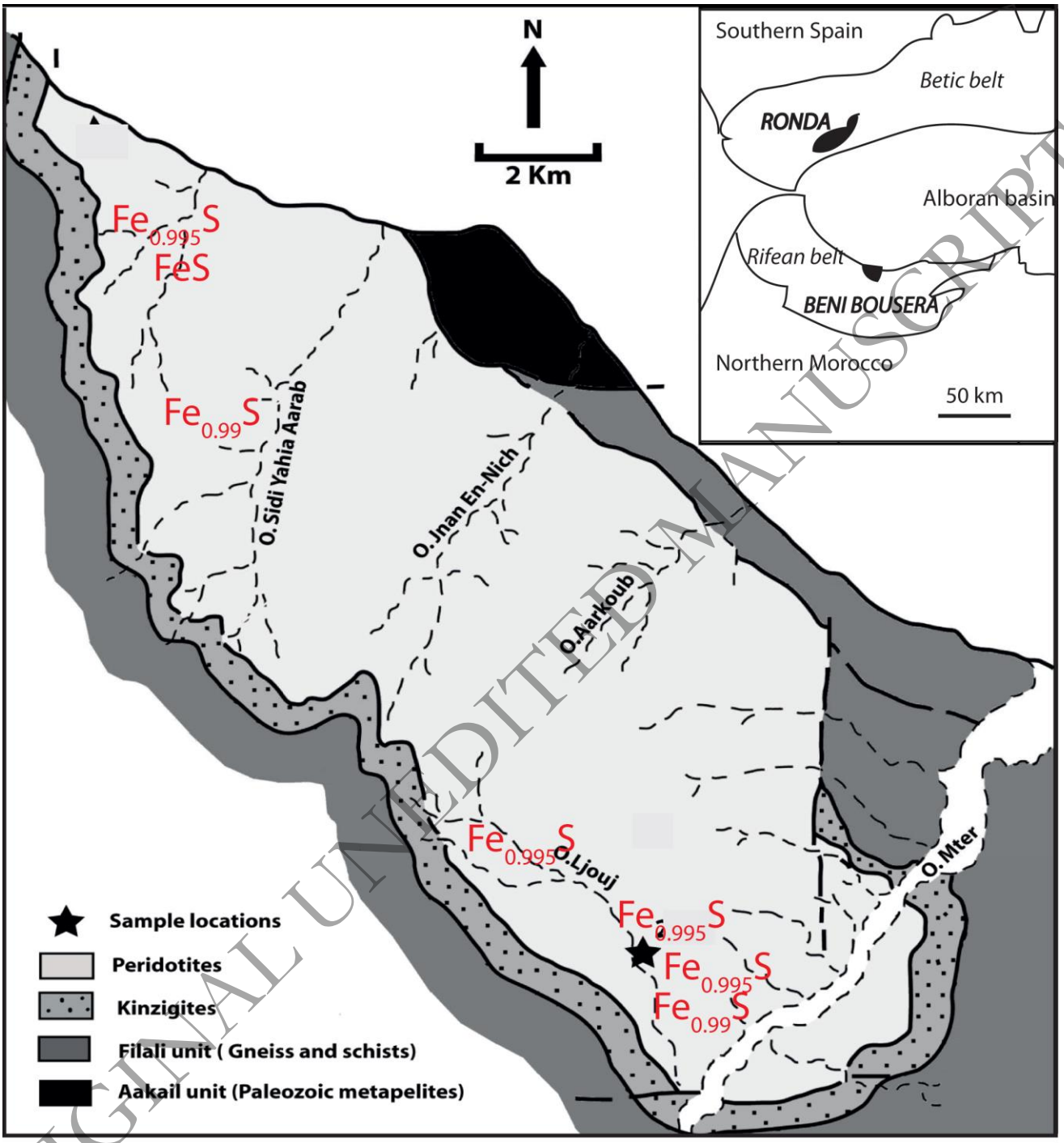

Fig. 1

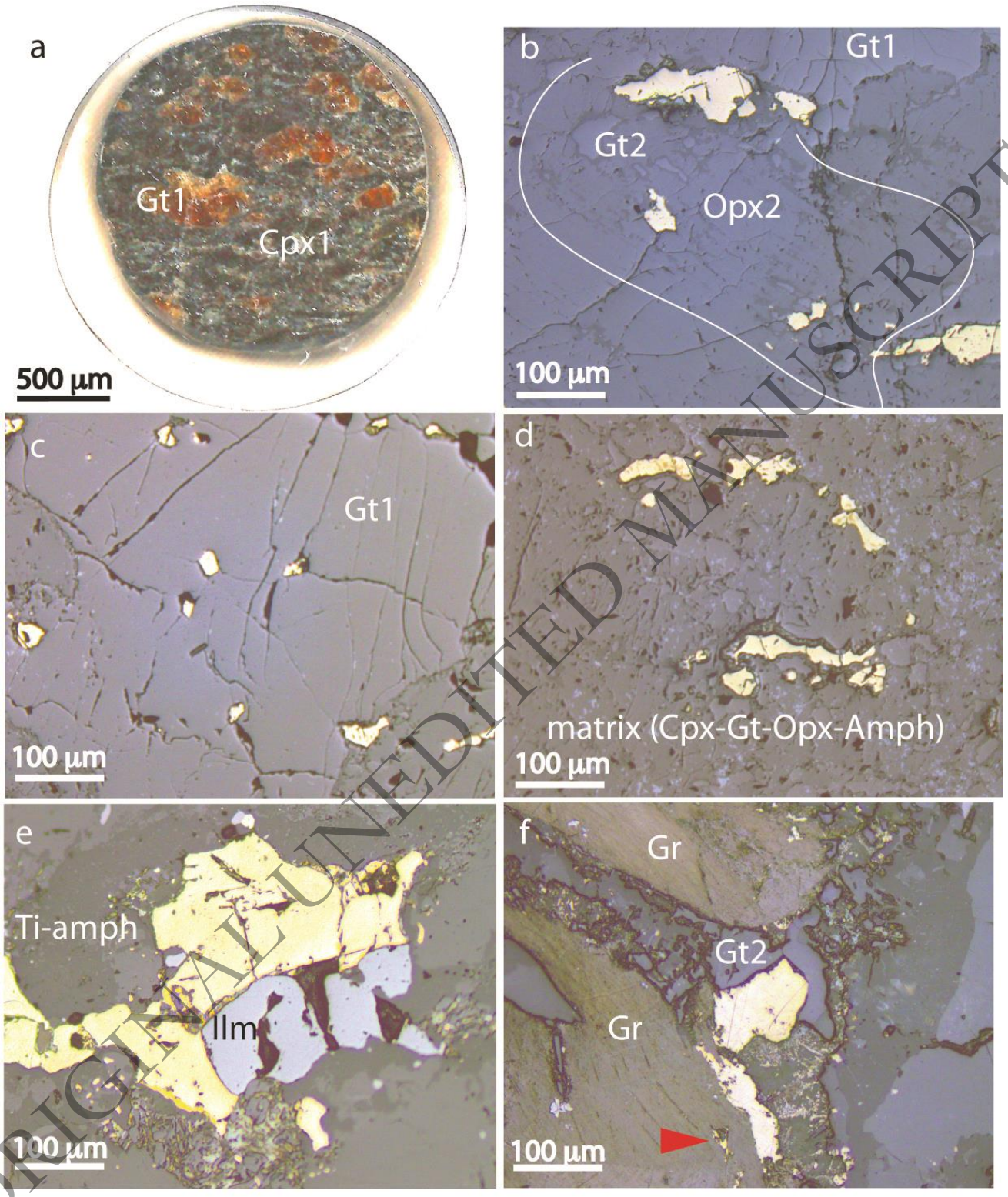

Fig. 2

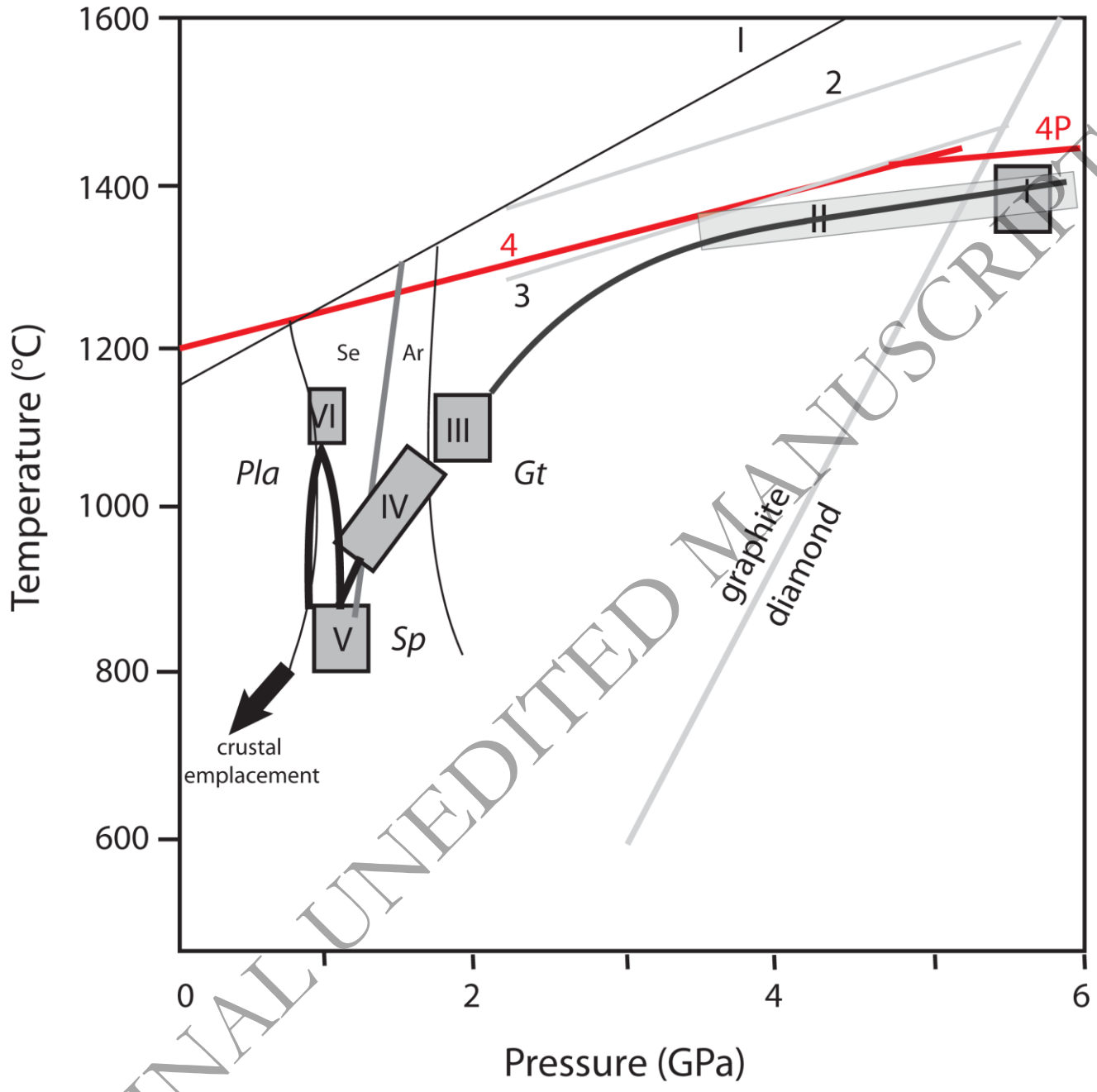

Fig. 3

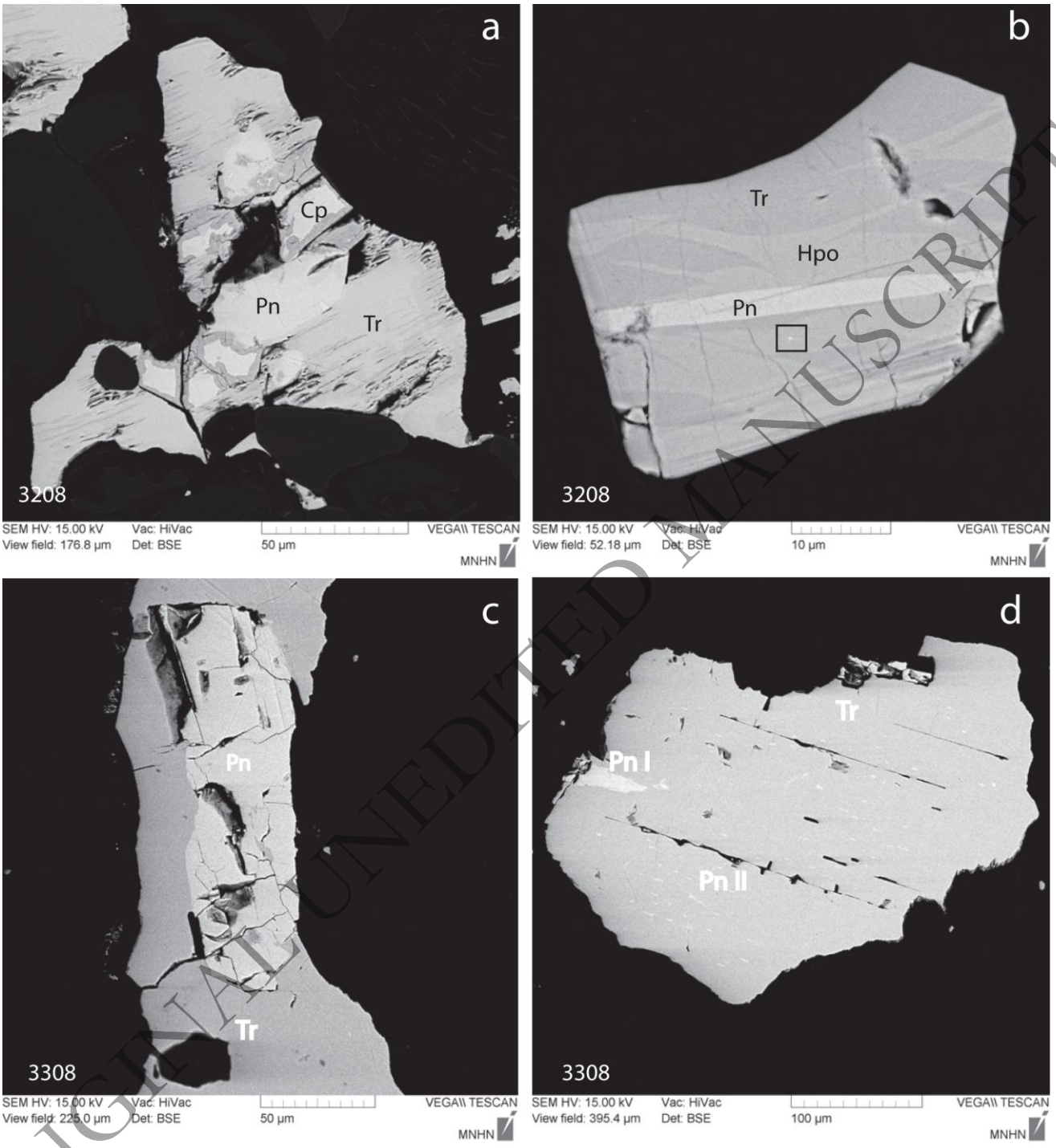

Fig. 4

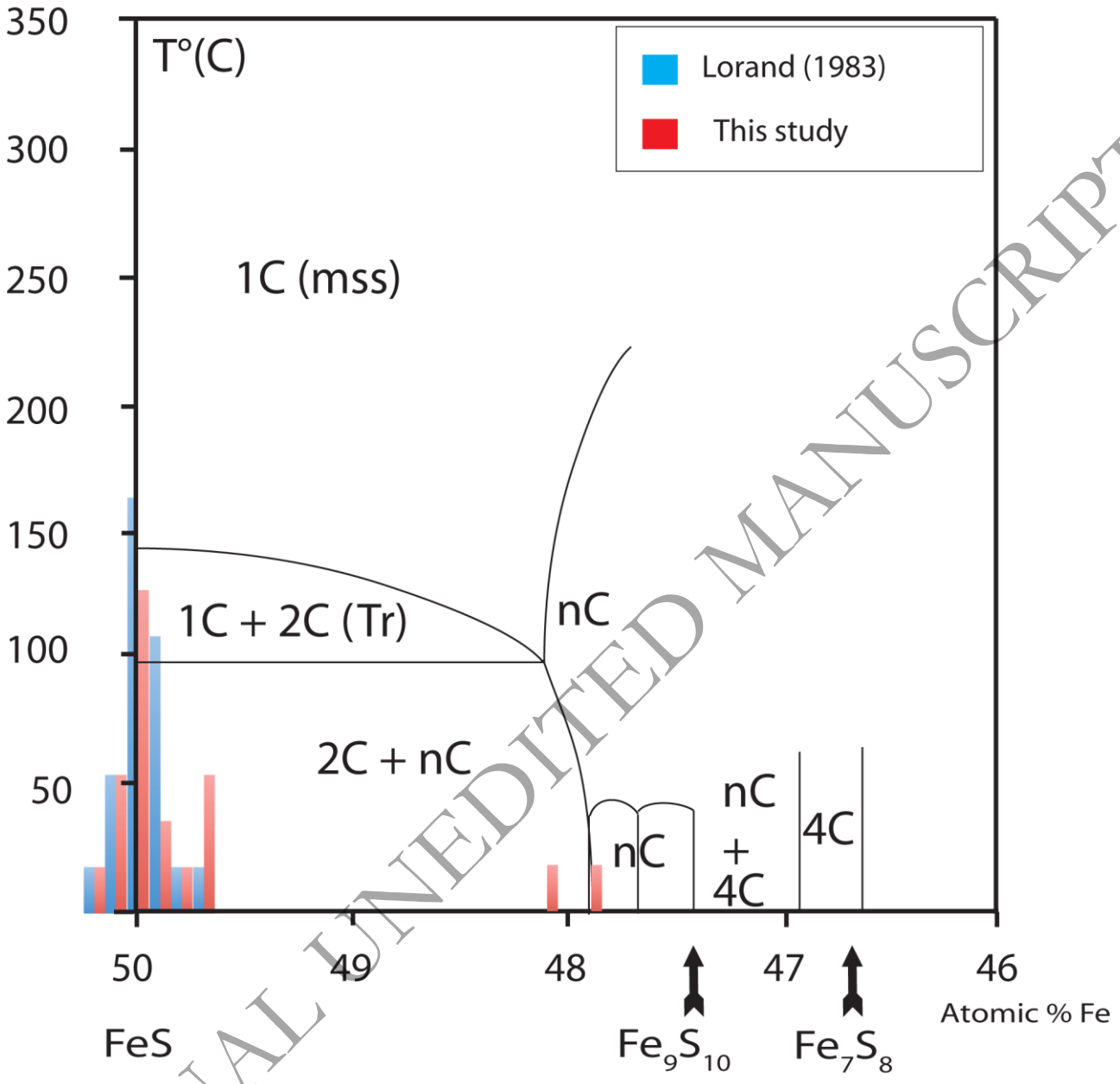

Fig. 5

Fig. 6

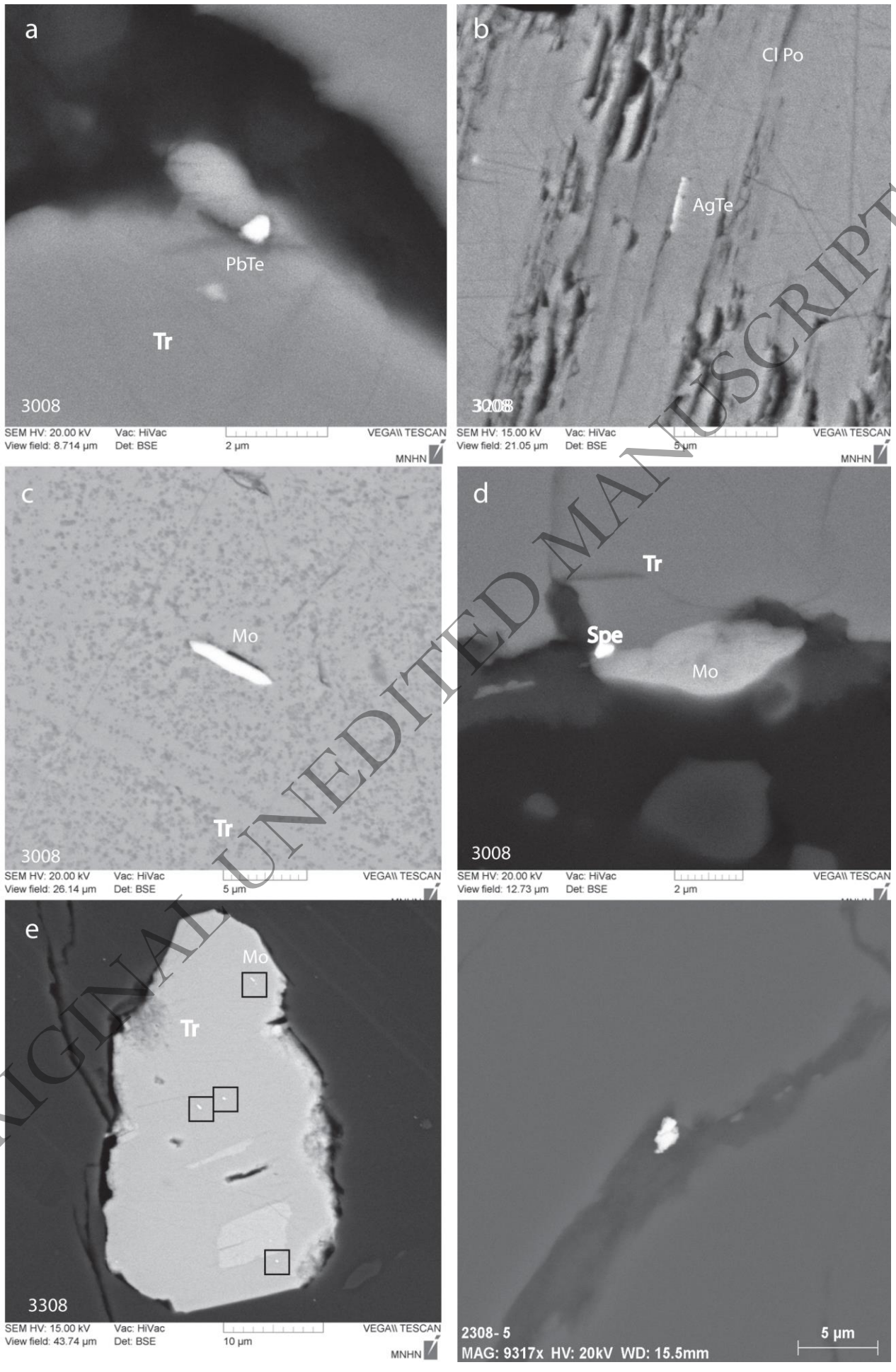

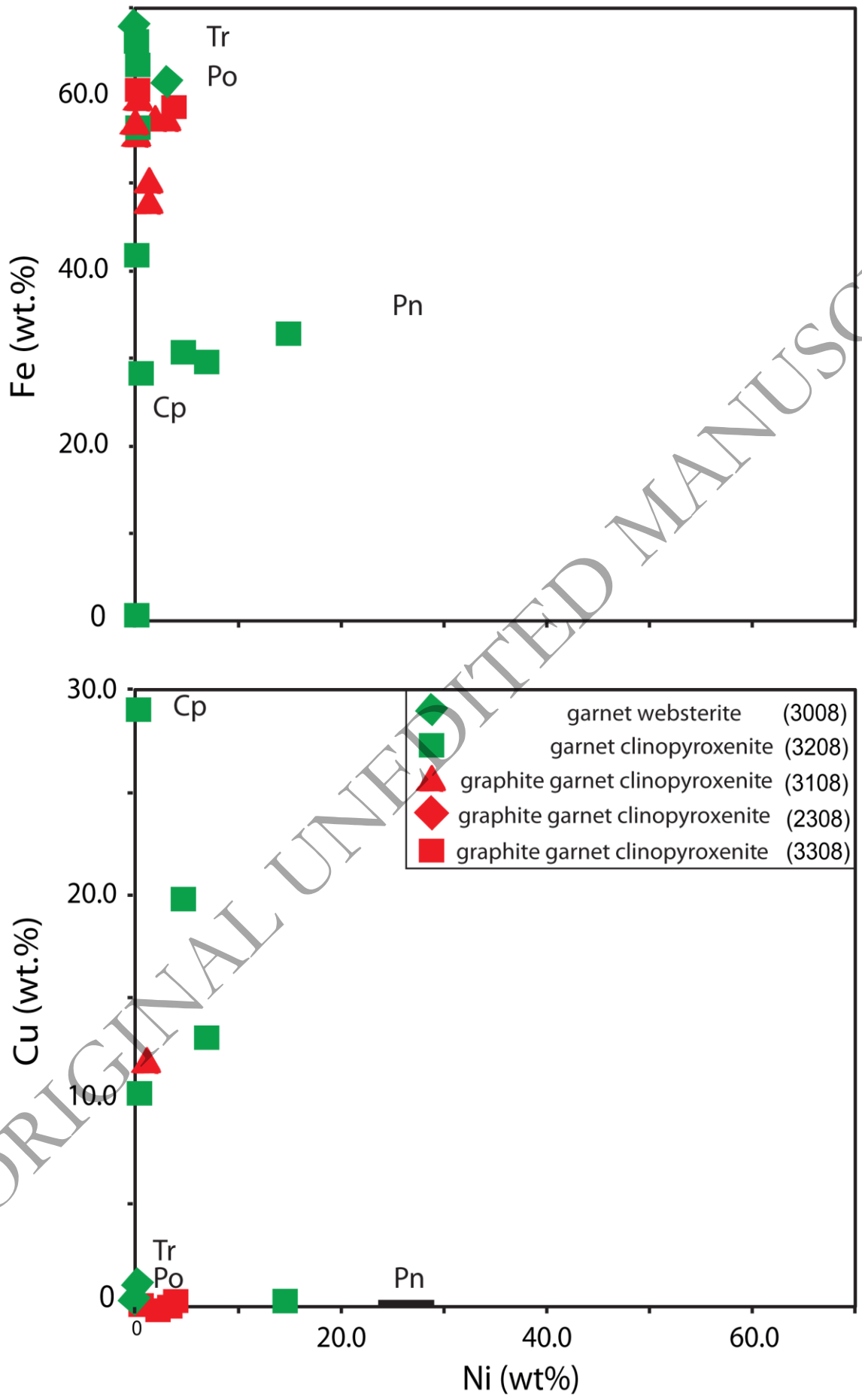

Fig. 7

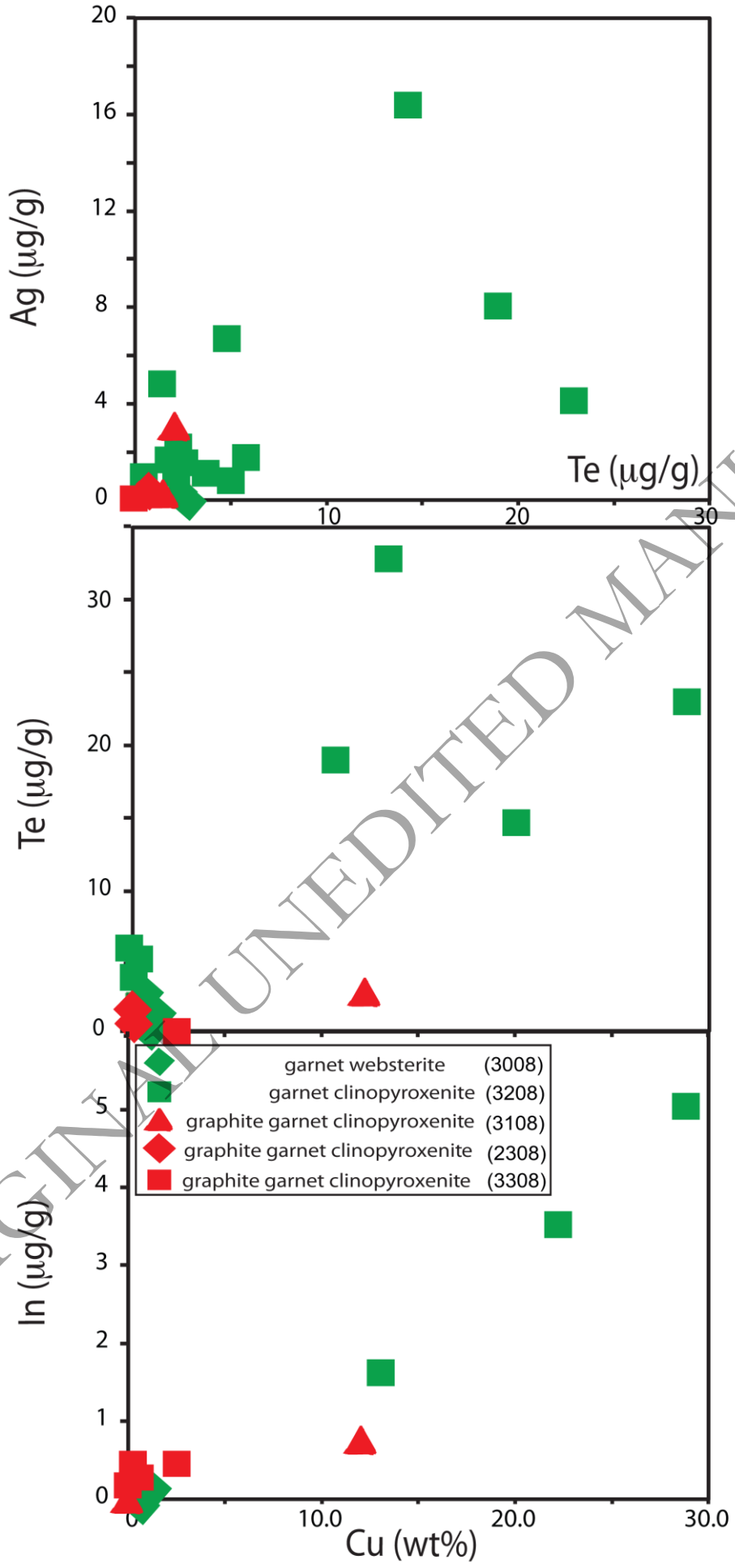

Fig. 8

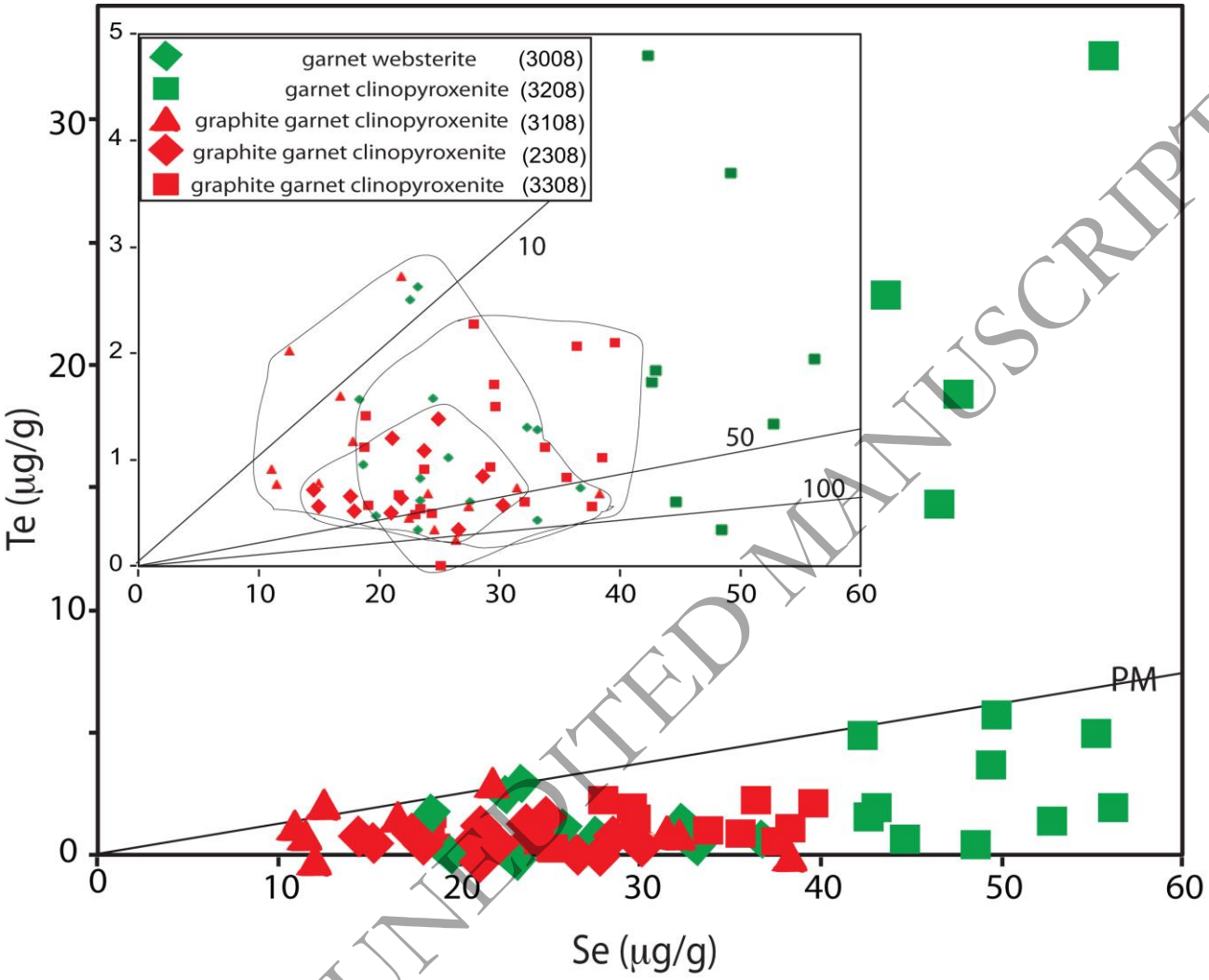

Fig. 9

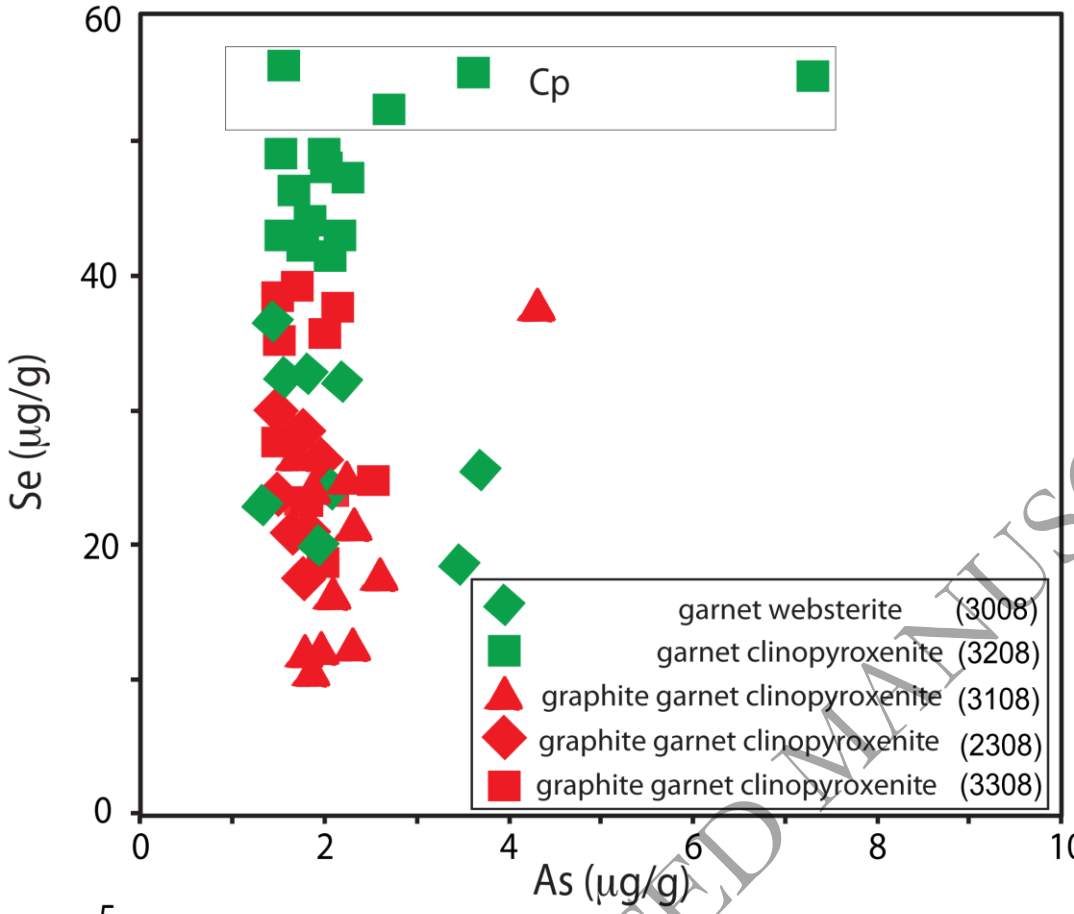

Fig. 10

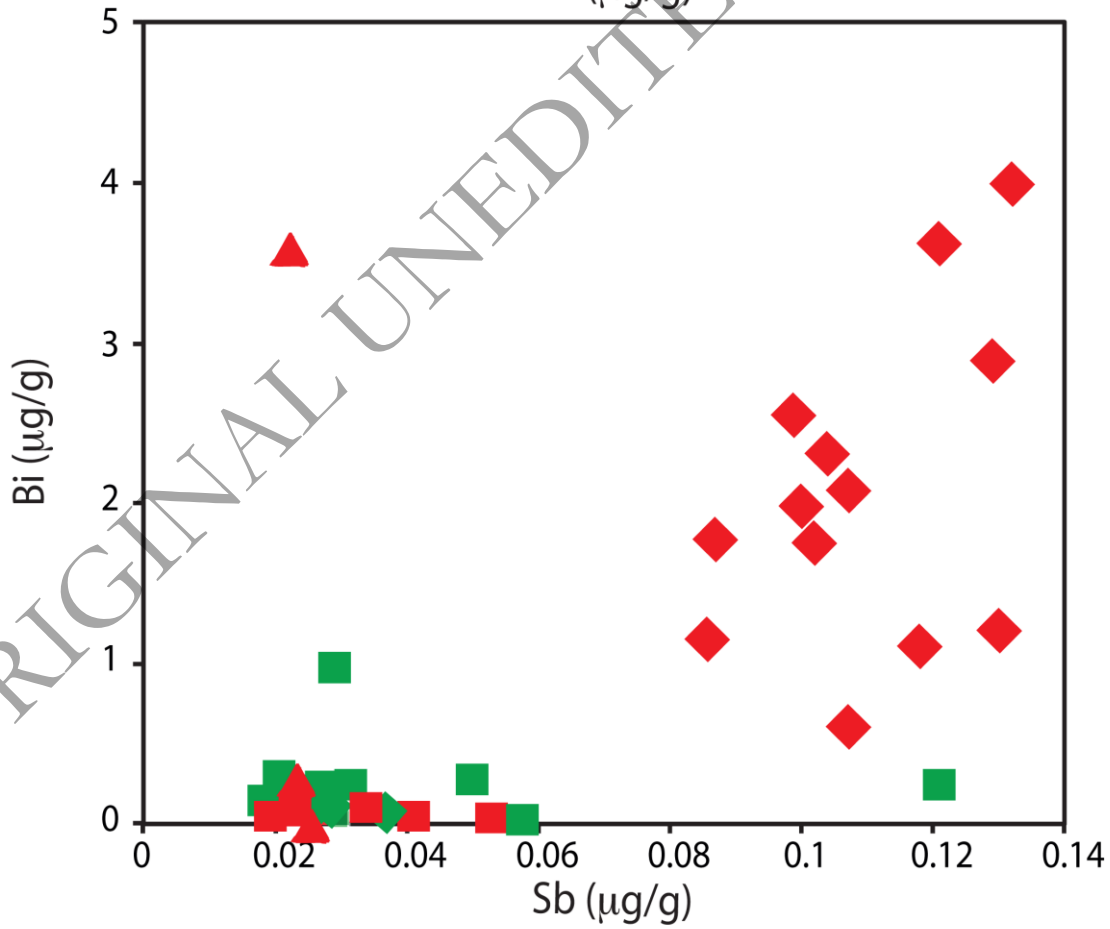

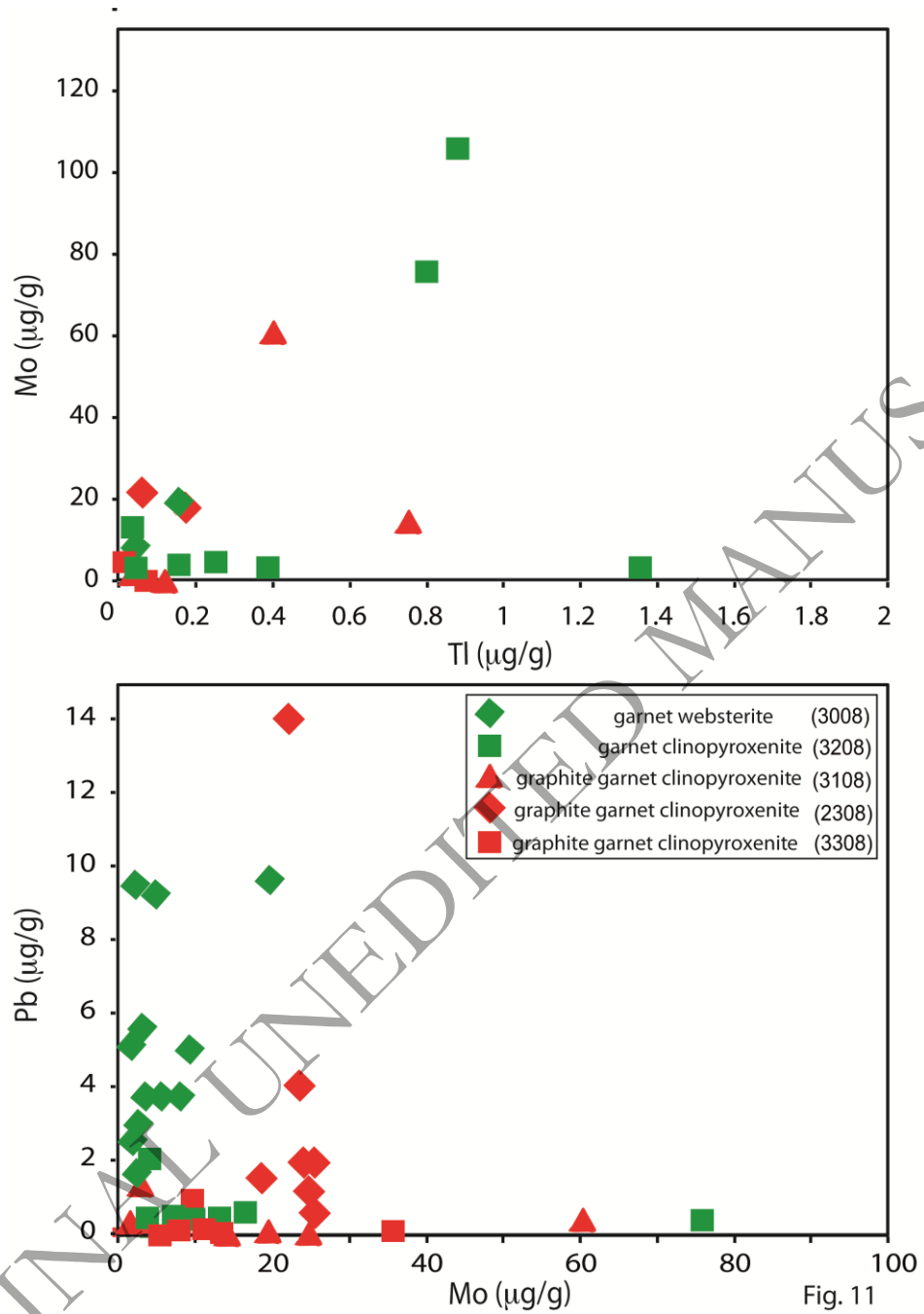

Fig. 11

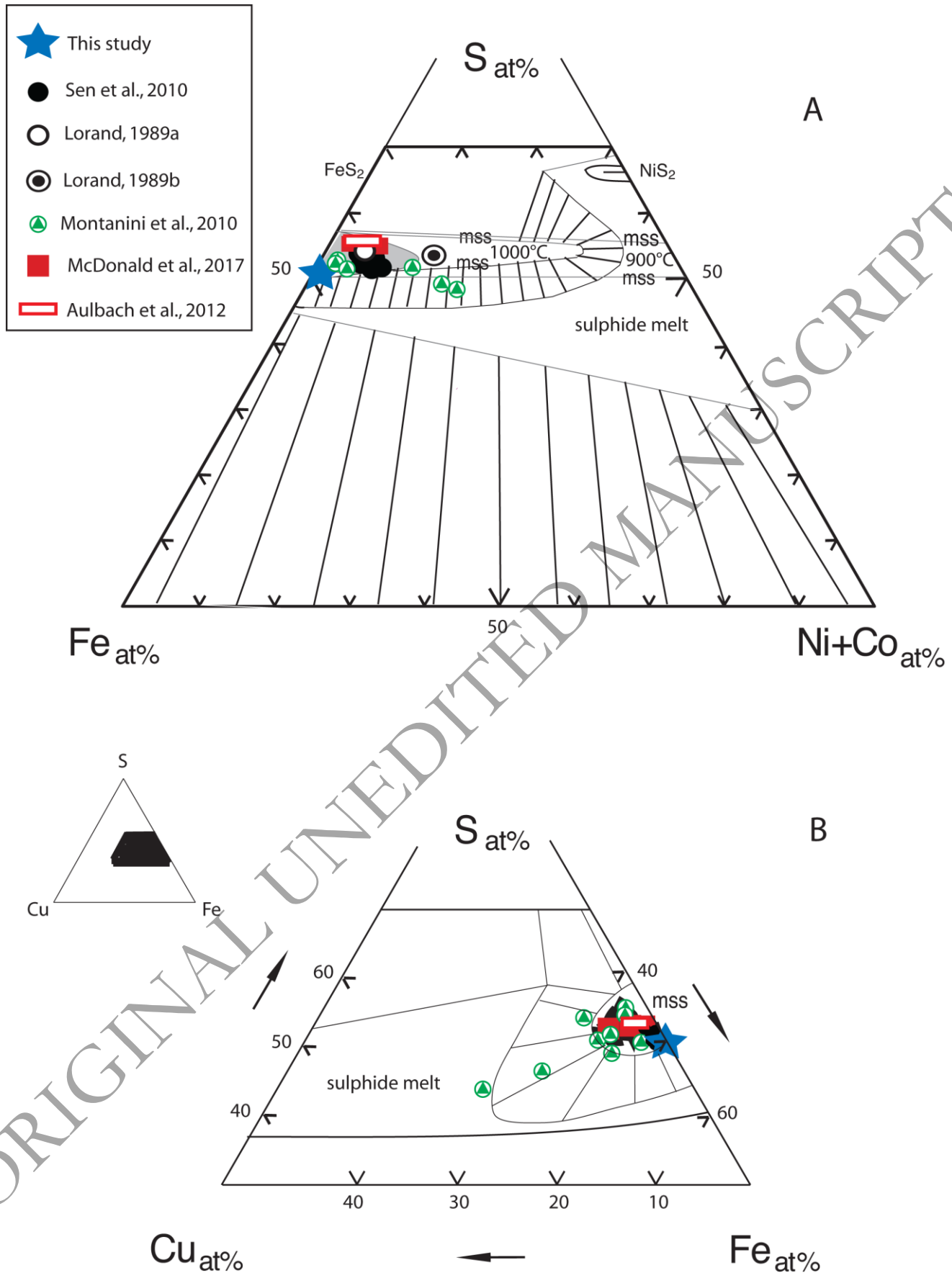

Fig. 12

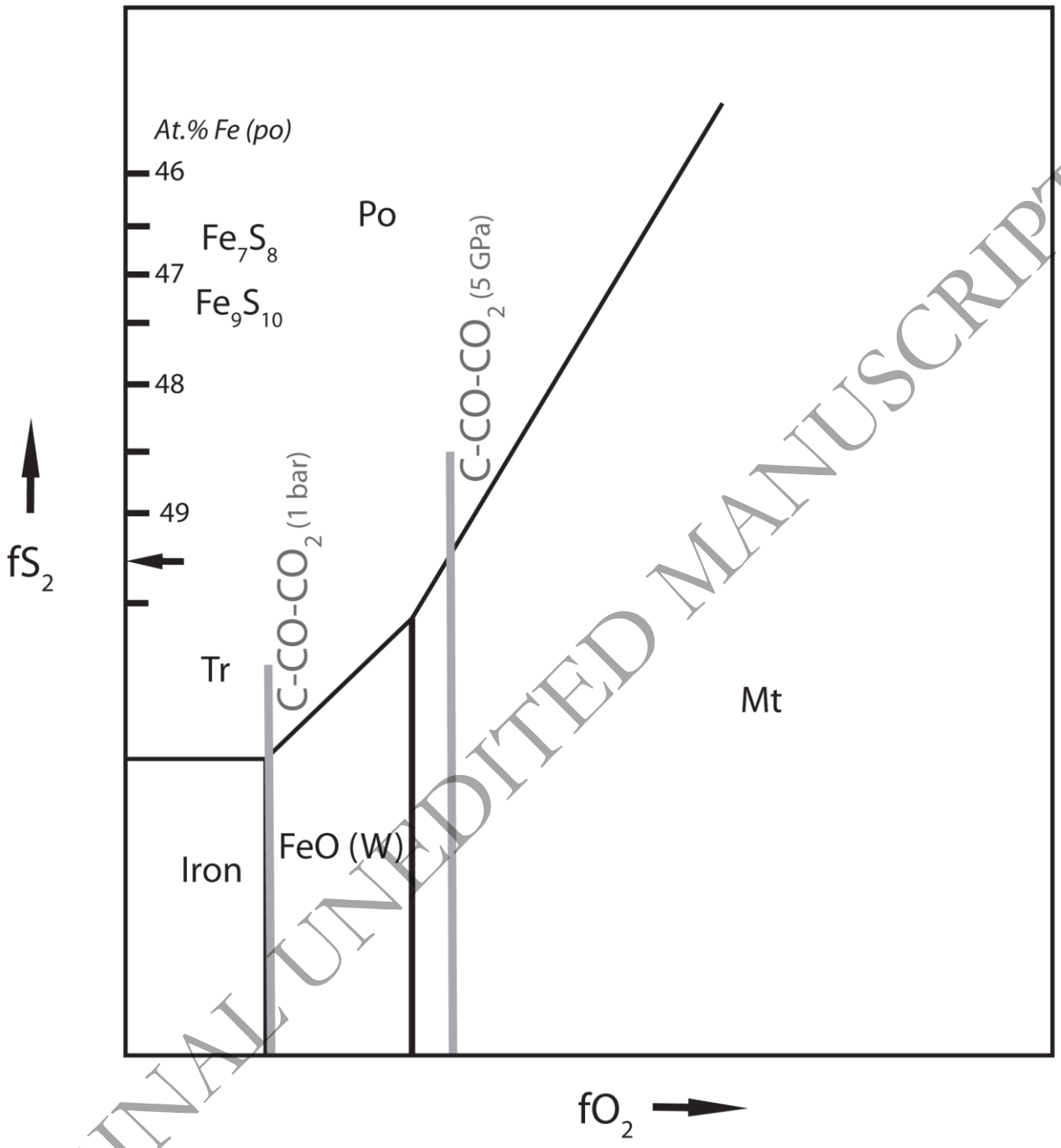

Fig. 13

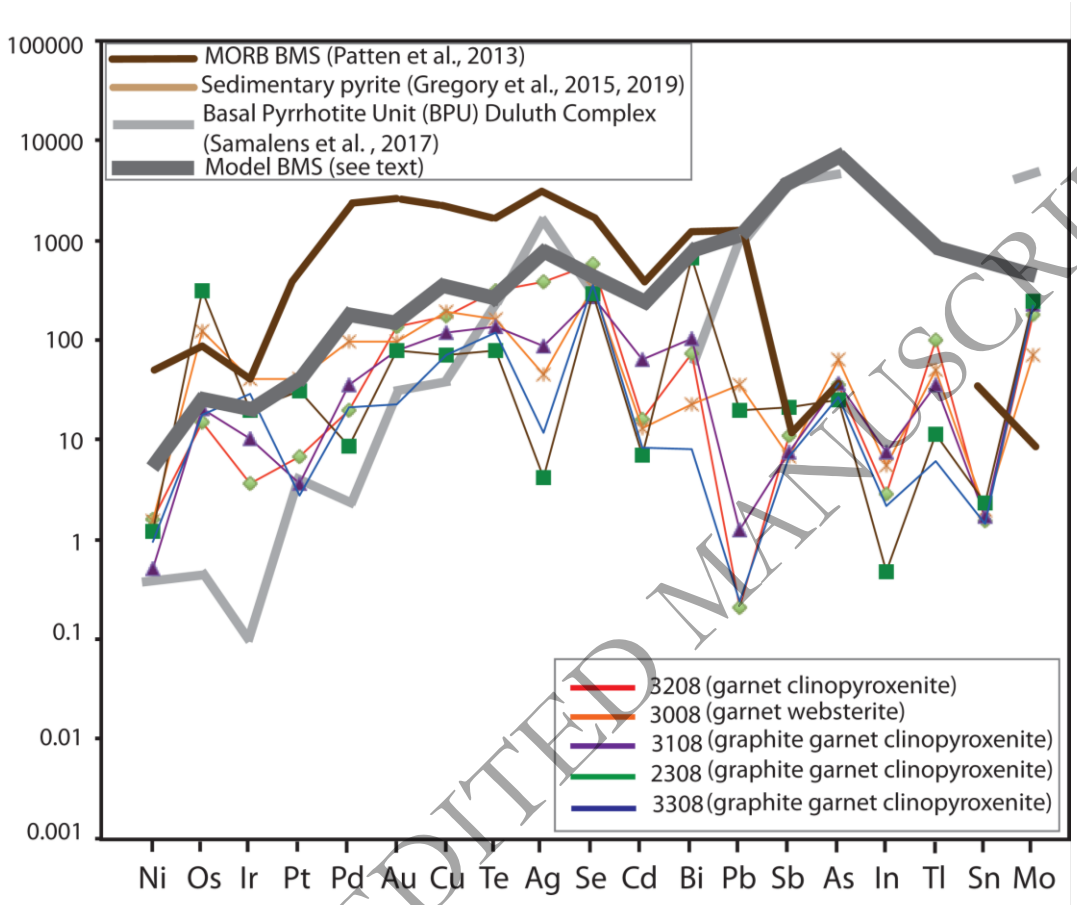

Fig. 14

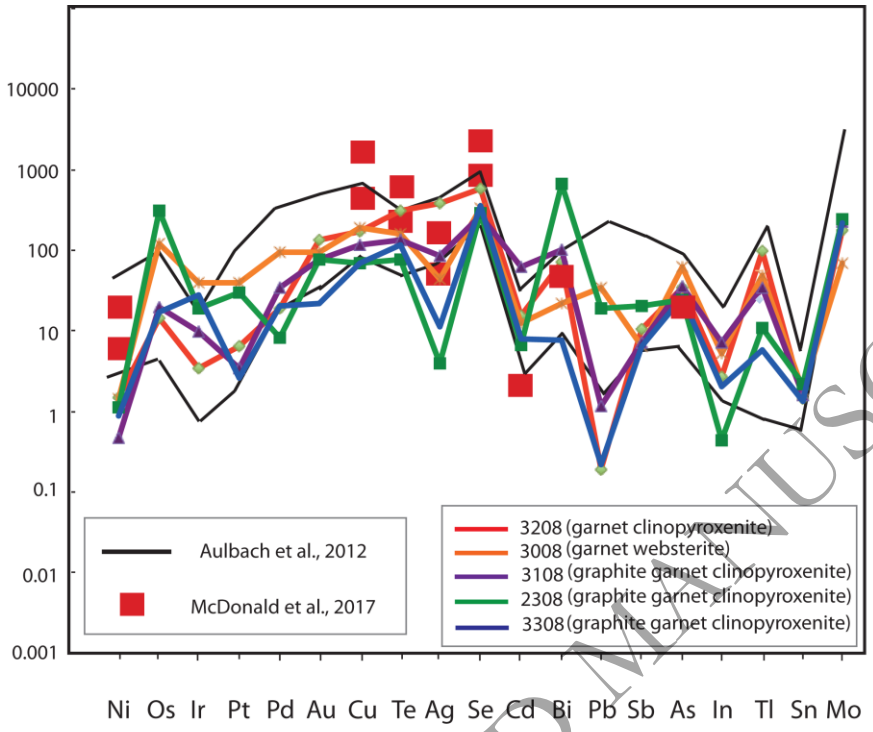

Fig. 15